NAVAL
POSTGRADUATE
SCHOOL

MONTEREY, CALIFORNIA

THESIS

TRANSPORT IMAGING OF MULTI-JUNCTION AND CIGS SOLAR CELL MATERIALS

by

Zi Xuan Ong

December 2011

Thesis Advisor:	Nancy M. Haegel
Second Reader:	Sherif Michael

Approved for public release; distribution is unlimited

THIS PAGE INTENTIONALLY LEFT BLANK

REPORT DOCUMENTATION PAGE		*Form Approved OMB No. 0704–0188*

Public reporting burden for this collection of information is estimated to average 1 hour per response, including the time for reviewing instruction, searching existing data sources, gathering and maintaining the data needed, and completing and reviewing the collection of information. Send comments regarding this burden estimate or any other aspect of this collection of information, including suggestions for reducing this burden, to Washington headquarters Services, Directorate for Information Operations and Reports, 1215 Jefferson Davis Highway, Suite 1204, Arlington, VA 22202–4302, and to the Office of Management and Budget, Paperwork Reduction Project (0704–0188) Washington DC 20503.

1. AGENCY USE ONLY *(Leave blank)*	2. REPORT DATE December 2011	3. REPORT TYPE AND DATES COVERED Master's Thesis
4. TITLE AND SUBTITLE Transport Imaging of Multi-Junction and CIGS Solar Cell Materials		5. FUNDING NUMBERS
6. AUTHOR(S) Zi Xuan Ong		
7. PERFORMING ORGANIZATION NAME(S) AND ADDRESS(ES) Naval Postgraduate School Monterey, CA 93943–5000		8. PERFORMING ORGANIZATION REPORT NUMBER
9. SPONSORING /MONITORING AGENCY NAME(S) AND ADDRESS(ES) National Science Foundation		10. SPONSORING/MONITORING AGENCY REPORT NUMBER

11. SUPPLEMENTARY NOTES The views expressed in this thesis are those of the author and do not reflect the official policy or position of the Department of Defense or the U.S. Government. IRB Protocol number ____N/A_____.

12a. DISTRIBUTION / AVAILABILITY STATEMENT Approved for public release; distribution is unlimited	12b. DISTRIBUTION CODE A

13. ABSTRACT (maximum 200 words)

Multi-junction solar cells are an emerging technology that improves the conversion rate of solar energy. Indium Gallium Phosphide (InGaP) is commonly used as the top cell in multi-junction cells grown on Germanium (Ge) or Gallium Arsenide (GaAs) substrates. To design more efficient solar cells using InGaP, it is important to characterize its transport parameters, particularly the minority charge carrier mobility, diffusion length and lifetime as a function of doping and material growth conditions.

In this work, transport imaging was performed on a set of InGaP heterostructures (with differing thicknesses, doping levels and minority carrier types) to determine their minority carrier diffusion length. These measurements, together with an independent set of time-resolved photoluminescence (TRPL) lifetime data, were used to calculate the minority carrier mobility values. For the shortest diffusion lengths, experimental limitations were encountered involving the finite carrier generation volume. Simulations were performed to explore the potential of modeling the convolution of diffusion behavior with a finite generation region to address these limitations.

Transport imaging was also performed on a set of Copper Indium Gallium Selenide (CIGS) materials. Polycrystalline CIGS represents an alternative to the expensive single-crystal InGaP. These initial experiments identified the challenges of applying transport imaging to polycrystalline materials.

14. SUBJECT TERMS Transport Imaging, Solar Cells, InGaP, CIGS, Minority Charge Carrier, Diffusion Length, Minority Charge Carrier Mobility	15. NUMBER OF PAGES 93
	16. PRICE CODE

17. SECURITY CLASSIFICATION OF REPORT Unclassified	18. SECURITY CLASSIFICATION OF THIS PAGE Unclassified	19. SECURITY CLASSIFICATION OF ABSTRACT Unclassified	20. LIMITATION OF ABSTRACT UU

Standard Form 298 (Rev. 8–98)
Prescribed by ANSI Std. Z39.18

THIS PAGE INTENTIONALLY LEFT BLANK

TRANSPORT IMAGING OF MULTI-JUNCTION AND CIGS SOLAR CELL MATERIALS

Zi Xuan Ong
Major, Singapore Armed Forces
B.Eng., Nanyang Technological University, 2005

Submitted in partial fulfillment of the
requirements for the degree of

MASTER OF SCIENCE IN COMBAT SYSTEMS TECHNOLOGY

from the

NAVAL POSTGRADUATE SCHOOL
December 2011

Author: Zi Xuan Ong

Approved by: Nancy M. Haegel
               Thesis Advisor

               Sherif Michael
               Second Reader

               Andres Larraza
               Chair, Department of Physics

iii

THIS PAGE INTENTIONALLY LEFT BLANK

ABSTRACT

Multi-junction solar cells are an emerging technology that improves the conversion rate of solar energy. Indium Gallium Phosphide (InGaP) is commonly used as the top cell in multi-junction cells grown on Germanium (Ge) or Gallium Arsenide (GaAs) substrates. To design more efficient solar cells using InGaP, it is important to characterize its transport parameters, particularly the minority charge carrier mobility, diffusion length and lifetime as a function of doping and material growth conditions.

In this work, transport imaging was performed on a set of InGaP heterostructures (with differing thicknesses, doping levels and minority carrier types) to determine their minority carrier diffusion length. These measurements, together with an independent set of time-resolved photoluminescence (TRPL) lifetime data, were used to calculate the minority carrier mobility values. For the shortest diffusion lengths, experimental limitations were encountered involving the finite carrier generation volume. Simulations were performed to explore the potential of modeling the convolution of diffusion behavior with a finite generation region to address these limitations.

Transport imaging was also performed on a set of Copper Indium Gallium Selenide (CIGS) materials. Polycrystalline CIGS represents an alternative to the expensive single-crystal InGaP. These initial experiments identified the challenges of applying transport imaging to polycrystalline materials.

THIS PAGE INTENTIONALLY LEFT BLANK

TABLE OF CONTENTS

LIST OF FIGURES

LIST OF TABLES

THIS PAGE INTENTIONALLY LEFT BLANK

LIST OF ACRONYMS AND ABBREVIATIONS

CCD   Charge Coupled Device

CIGS   Copper Indium Gallium Selenide

CL   Cathodoluminescence

EBIC   Electron-Beam-Induced Current

GaAs   Gallium Arsenide

InGaP   Indium Gallium Phosphide

InP   Indium Phosphide

ISR   Intelligence, Surveillance and Reconnaissance

PL   Photoluminescence

SEM   Scanning Electron Microscope

SNR   Signal-To-Noise Ratio

TRPL   Time-Resolved Photoluminescence

UAV   Unmanned Aerial Vehicle

THIS PAGE INTENTIONALLY LEFT BLANK

ACKNOWLEDGMENTS

The author would like to express his most sincere appreciation and gratitude to his thesis advisor, Professor Nancy Haegel, for her invaluable advice and guidance throughout the entire course of the work. Her continual support and encouragement have been a very great motivational factor, without which the thesis would not have been able to be completed successfully.

The author would also like to extend his appreciation to MAJ David J. Phillips (United States Army) and MAJ Yoseoph Seo (Republic of Korea Army) for their immense support and help with the laboratory equipment during this time. The many enriching discussions have also proved invaluable and have thus enabled the project to proceed smoothly.

Lastly, the author would like to thank his wife, Weiling, who has stood unwavering by his side and never doubting in his endeavors. A strong lady who had to take up the burden of caring for the big boy and their toddler girl, while carrying another one inside of her during the time of writing.

THIS PAGE INTENTIONALLY LEFT BLANK

I.   INTRODUCTION

A.   SOLAR CELL TECHNOLOGY

The expanding use of solar cell technology promises a source of energy that is environmentally friendly, renewable, and most importantly, lasting. In this era, there is an ever-increasing power consumption requirement to fuel the global economy and its operations. While fossil fuel continues to be the mainstay of energy providers, this energy source is not limitless and will eventually be depleted. In addition, the by-products of burning fossil fuel contribute significantly to pollution, which subsequently harms the eco-system in which we live. As such, solar energy can serve as a viable option for replacing fossil fuel, in part if not in whole, with fewer of its detrimental effects.

While solar energy presents immense potential, there are challenges to how we can effectively tap this energy source. The first solar cell was developed by Charles Fritts in the 1880s. At its earliest stage, it could effectively convert only less than 1% of the incident light [1]. As technology progressed, current single-junction solar cells are now able to attain a conversion rate of approximately 10 to 20%, with the highest efficiency record held at 27.6% [2]. Conversion efficiency remains an important issue when considering the adoption of solar cells on a large scale. The existing conversion rate makes solar cells less efficient and requires more panels to meet a given requirement. This, in turn, drives the implementation cost up, making it less appealing as a substitute for traditional fossil fuel. The aim for solar cell research is therefore to simultaneously raise the limit of conversion efficiency and drive down manufacturing costs.

Solar cells are photovoltaic devices that absorb sunlight and convert the energy from the electromagnetic spectrum into usable electricity via the photovoltaic effect. Designed essentially as semiconductors with p-n junctions, free charge carriers are created within the material with the absorption of incident light. To achieve high conversion efficiency, these charges will need to be

efficiently transported out of the bulk material before they are lost, primarily due to the generation-recombination effect. The ability of these charges to be transported is primarily dependent on the diffusion length of minority carriers. The time that a minority charge carrier exists before it recombines is known as the lifetime, and the distance that the charge travels in its lifetime, based on its diffusivity, is called the diffusion length. Based on lifetime and diffusion length, the mobility of the electron or hole in the lattice can be determined, thus allowing better understanding of the diffusivity of the minority charge carriers in a material.

There are many challenges to building an efficient solar cell. Key parameters in characterizing solar cells start with the material charge transport parameters, namely the charge mobility, lifetime and diffusion length. It is the goal of every solar cell manufacturer to maintain high carrier lifetime so as to realize long diffusion lengths. Long diffusion lengths ensure that the charges, generated from the incident light, can effectively travel through its generation region to reach the depletion region where they can be collected. Thus, being able to accurately determine the diffusion length of any solar cell material proves advantageous by providing insights for the future design and manufacture of a highly efficient solar cell. A rapid characterization tool that can determine the diffusion length directly following material growth could be very valuable.

B.   PURPOSE OF THESIS

The objective of this thesis is to determine the minority carrier diffusion length and mobility of several Indium Gallium Phosphide (InGaP) materials for use in multi-junction solar cells. This will be done through transport imaging, a contact-free, optical technique that directly images the minority carrier diffusion within the samples. The method uses a scanning electron microscope (SEM) coupled with an optical microscope to image the recombination luminescence due to charge motion. From the images, the minority carrier diffusion length can be easily extracted. Together with independent carrier lifetime data, determined by time-resolved photoluminescence (TRPL), the carrier mobility can be calculated.

2

The determination of these key material charge parameters will enable the full characterization of the solar cell materials and provide a better understanding as to the performance of the solar cells. Furthermore, direct measurements of the behavior of minority carriers in InGaP are limited and experimental data on the mobility of these carriers are also scarce in existing literature. The work done in this thesis will provide an opportunity to investigate and further determine experimental values of such carriers in the solar cell samples.

C.   MILITARY RELEVANCE

Power sources are an essential part of any military operations, especially in the current context where reliance on machineries and systems is becoming more prevalent. In order to sustain such operations, long logistical trains have to be established for the supplying of sufficient energy. To add to the complication, operations nowadays also tend to occur far away from the home base, posing serious challenges to the current modus operandi of logistical support in terms of energy. What is needed is a new fuel alternative that is renewable and can be carried by the front-line troops, making them self-sustainable. Efficient solar cell devices can be one answer to this problem.

Ray Mabus, the U.S. Secretary of Navy, has commented that there is now, more than ever, an impetus for the U.S. military to look at renewable energy [3]. This issue has implications at both the strategic and tactical levels. Strategically, traditional fossil fuel can, most often, only be bought from regions which are either volatile or have the potential to become so. Any sovereign state's reliance on such fuel sources creates an extreme vulnerability to its overall national security. Tactically, it is highly costly to supply such fossil fuel to front-line troops. The cost is not only in a monetary sense, but also involves the lives of soldiers or Marines lost in trying to bring these fuels into the theater of operation. By adopting solar energy, a state is free of geo-political constraints at the strategic level. At the tactical level, ground commanders can be assured of self-sustainability without having to be duly concerned with or crippled by the lack of logistical support for energy.

3

For Singapore, the energy issue is also of major concern to both its political and military leaders. Being a small island state without any natural resources, it can only look to foreign parties for the acquisition for such energy sources. As discussed earlier, this results in a national-level vulnerability that has to be addressed. While Singapore enjoys good ties with countries both regionally and globally, being self-sufficient remains a priority in the city country's development plan. Solar energy will prove a hopeful alternative to meet that end.

Another area in which solar energy proves useful is the space arena. More and more states are embarking on space programs, which seek to put satellites up in space. For the military, such satellites play in an important role for communications as well as intelligence, surveillance and reconnaissance (ISR) purposes. These satellites are usually in geo-synchronous orbits and are constantly exposed to the sun. Multi-junction solar cells provide a feasible means of power generation that is both stable and cost effective.

D.   THESIS OVERVIEW

Chapter I begins by giving a brief introduction to solar cell technology and its current state of development. It also outlines the purpose of this thesis and the work to be done. Finally, it evaluates the relevance of solar cell technology as applied to the military.

Chapter II presents background information on multi-junction solar cells using InGaP and how they work. The basic concepts of semiconductor parameters, such as minority carrier mobility, lifetime and diffusion length, are reviewed in greater depth.

Chapter III explains the technique of transport imaging. It also describes the setup of the laboratory equipment as well as the experimental procedures for applying the technique to the samples.

Chapter IV summarizes the results obtained from the experiments and provides the analysis of the results. It also highlights the experimental limitations encountered involving finite generation volume for charge carriers for the samples with short diffusion lengths.

Chapter V explores a deconvolution method to overcome the limitations encountered for finite charge carrier generation volume. The deconvolved results are evaluated and compared against the initial results.

Chapter VI introduces the Copper Indium Gallium Selenide (CIGS) material system as an alternate type of solar cell. The results of an initial investigation of the transport imaging measurement of CIGS are presented. Some of the challenges of applying the transport imaging technique on CIGS are also identified.

Finally, Chapter VII concludes the report with a summary of the work done and gives the direction for which future research relating to the thesis can be carried out.

THIS PAGE INTENTIONALLY LEFT BLANK

II.   BACKGROUND

A.   MAJORITY AND MINORITY CHARGE CARRIERS IN SEMICONDUCTORS

In all crystalline structures, the interactions of atoms or molecules within the crystal lattice result in discrete energy levels, which combine to form energy bands. In semiconductors, the lower occupied energy bands are known as the valence bands while the higher ones are known as the conduction bands. In between the conduction and valence bands is a range of forbidden energy levels called the band-gap. Within the valence band, the electrons are bound by energy bonds to their parent atoms in the crystal lattice.

When an electron gains enough energy, either through thermal excitation or photon absorption, it is possible for the electron to break free of its chemical bonds and make an upward transition to the conduction band. The condition for this to happen is that the energy gained, ΔE, must be greater than or equal to the band-gap energy, E_g, i.e., the energy needed for it to cross the forbidden band-gap ($\Delta E \geq E_g$). The electron is then said to have make a "quantized jump." After the transition, there is a vacancy left behind in the valence band by the electron, called a hole. This is the generation of an electron-hole pair (Figure 1). Both the electron, negatively charged, and the hole, positively charged, can then move freely within their respective bands, especially under the influence of an applied electric field. The term "charge carrier" is used to refer to both the electrons and holes.
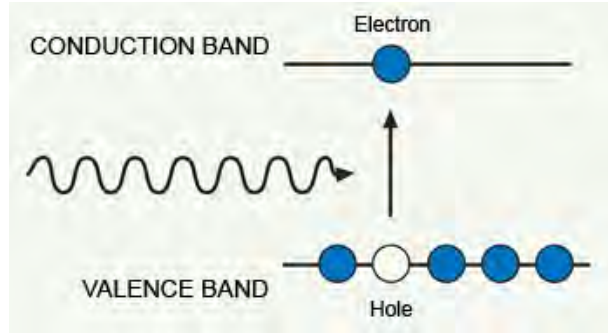
Figure 1.   Generation of Electron-Hole Pair (After [4])

An intrinsic, or pure, semiconductor will have an equal number of electrons and holes across the band-gap under steady state thermal equilibrium. The reason for this is that electrons and holes are always created in pairs. The charge carrier (electron or hole) concentration is governed by the following equation:

$$n_0 p_0 = n_i^2 \qquad \text{(Eq. 1)}$$

where n_0 is the electron charge carrier concentration, p_0 is the hole charge carrier concentration and n_i is the average intrinsic charge carrier concentration.

To improve and control the conductivity of the semiconductor, the doping process, which is the intentional introduction of impurities, is often performed on the material. In this case, the semiconductor now becomes extrinsic. Doping can either be done with donor or acceptor dopants.

Donor dopants (e.g., Group V elements for doping of Si) have one extra electron than is required for bonding with the surrounding atoms in the crystal lattice. As such, an electron is deemed have been 'donated' and is free to move in the conduction band. On a macro scale, the overall concentration of electrons will now be greater than the concentration of holes $(n_0 > p_0)$ at room temperature. The electrons, being of higher concentration, are called the majority charge carriers, and the holes, being of lower concentration, are called the minority charge carriers. The semiconductor material is now referred to as an n-type material (Figure 2).
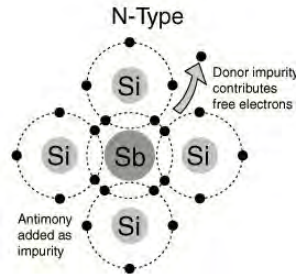
Figure 2.   Example of a N-Type Material (Silicon Doped with Antimony) (From [5])

Acceptor dopants (e.g., Group III elements for doping of Si) have one less electron than is needed for bonding. They will then readily 'accept' a nearby electron, creating an extra hole in the process (Figure 3). Again, on a macro level, this causes the concentration of holes to be greater than the concentration of electrons ($p_0 > n_0$) at room temperature. Therefore, the holes are now the majority charge carriers while the electrons are the minority charge carriers, and the semiconductor material is known as a p-type material.
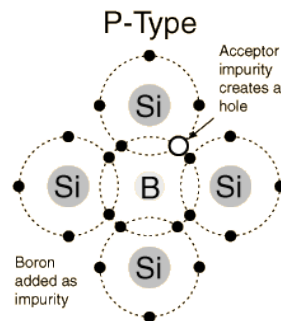
Figure 3.   Example of a P-Type Material (Silicon Doped with Boron) (From [5])

The behavior of minority charge carriers, rather than the majority charge carriers, is more often the primary concern of semiconductor manufacturers or solar cell designers. When exposed to photons with energy $E \geq E_g$, both types of charge carriers are generated (electron-hole pair generation). For both n-type and p-type materials, the change in concentration for the majority carrier due to

the excitation is generally very small because of its large existing carrier population. On the other hand, the fractional change in concentration for the minority carrier is considerably more significant in comparison. As a result, minority charge carriers play a more critical role in determining the non-equilibrium electrical properties of the material, making it an important parameter for consideration.

B.   CHARGE CARRIER DIFFUSION LENGTH

Diffusion, in general, is the migration of particles from a region of higher concentration to a region of lower concentration. It is akin to the spread of a drop of ink in a glass of water or the molecular spreading of a gas in a container [6]. When a semiconductor is exposed to illumination, generation of electron-hole pairs occurs. This is usually localized, resulting in a region which suddenly experiences a higher concentration of charge carriers than the surrounding material. This difference in concentration creates a concentration gradient and causes the charge carriers to diffuse into the immediate vicinity. Figure 4 shows the migration of the charge carriers away from the center point of illumination, smoothing out the concentration gradient over time. For majority carriers, there only need be a small change to the local concentration to accommodate the flux of the diffusing carriers, whereas there is a more significant change for the minority carriers. Once again, the importance of understanding minority carrier diffusion in semiconductors is highlighted.
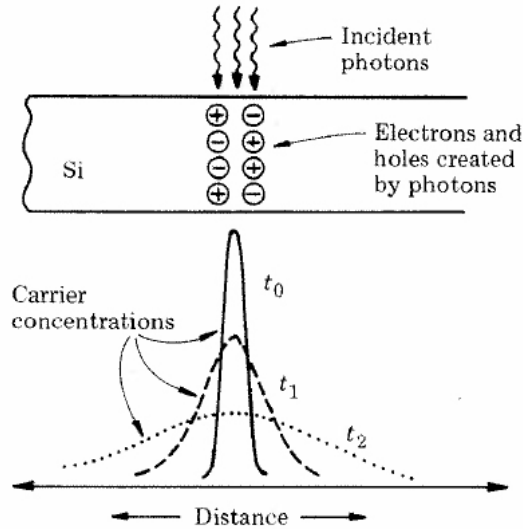
Figure 4.   Charge Carrier Diffusion. The top Portion Shows the Generation of Electron-Hole Pairs due to Incident Light. The Bottom Portion Shows the Broadening of the Carrier Distribution Over Time (From [6])

The diffusivity of charge carriers within a material is described by the diffusion coefficient, D. This coefficient is governed by the Einstein relation as given below:

$$D = \frac{\mu k T}{e}$$
(Eq. 2)

where μ is the charge carrier mobility, k is Boltzmann's constant, and T is the temperature. An important thing to note is that the mobility value for electrons and holes are different even if within the same material. This is due to their difference in size and mass and also as a result of their transport in different bands. Therefore, the diffusion coefficients for electrons and holes are also different.

The diffusion length is defined as the average length a charge carrier, be it electron or hole, is able to diffuse before it recombines and returns to its equilibrium state. The diffusion length, L_{diff}, can be calculated by the following equation:

11

$$L_{diff} = \sqrt{D\tau} = \sqrt{\frac{\mu \tau kT}{e}} \qquad \text{(Eq. 3)}$$

where is D the diffusion coefficient as defined earlier, and τ is generally the minority charge carrier lifetime.

C.   CHARGE CARRIER MOBILITY

The mobility is a measure of the relative ease with which a charge carrier can move within a material. In general, the mobility, μ, can be found by:

$$\mu = \frac{e\tau_s}{m^*} \qquad \text{(Eq. 4)}$$

where e is the electron charge, τ_s is the scattering lifetime and m^* is the effective mass. The difference in mobility between electrons and holes can be explained by the fact that electrons and holes have different effective masses, resulting in different mobility values.

Mobility of minority charge carriers is traditionally determined by the Haynes-Shockley technique [7]. In the experiment, a pulse of charge carriers is created at one end of the semiconductors (usually done by having light incident on it). Under an applied electric field, the charge carriers will be made to move across the length of the semiconductor to the other end. Using an oscilloscope, the transit time can be found. The velocity of the carrier can then be easily calculated since the distance traveled (which is equal to the length of the semiconductor) and the transit time is known. The mobility is defined as the proportionality constant between the applied electric field, E, and the drift velocity, v:

$$\mu = \frac{v}{E} \qquad \text{(Eq. 5)}$$

The disadvantages to this technique are that contacts have to be added to the semiconductor to induce the needed electric field and that it averages over the full length of the sample.

The mobility can be influenced by both temperature and the doping level of the semiconductor. As the charge carriers move through the material, they can be scattered by the atoms vibrating about their fixed positions in the crystal lattice. When temperature increases, the atoms gain more kinetic energy and the vibrational displacement increases. This causes a higher possibility of collision between the charge carriers and the vibrating atoms, affecting the mobility. With regard to doping, charged ions are introduced to the lattice in place of neutral atoms. The charge of the ions has either an attractive or repulsive effect on the moving charge carriers, acting to deflect and scatter them, thereby affecting the mobility. Hence, the mobility is, in certain temperature regimes, inversely proportional to the doping level.

D. CHARGE CARRIER LIFETIME

The carrier lifetime is the mean time that a carrier exists before it recombines and disappears. A non-equilibrium charge carrier does not exist forever. As it travels through the bulk material, it will eventually encounter an opposite charge carrier (e.g., an electron meeting a hole) and recombine with it. Therefore, for the minority carriers, the lifetime is commonly inversely proportional to the population of the majority carriers:

$$\tau = \frac{B}{N}$$
(Eq. 6)

where B is the recombination coefficient and N is the majority carrier population.

Charge carrier lifetime can be determined through the time-resolved photoluminescence (TRPL) technique [8]. A variety of configurations for TRPL exist, but generally, the semiconductor sample is excited with a pulsed external illumination source and the subsequent photoluminescence (PL) against time profile of the semiconductor is observed and recorded. The lifetime can be evaluated from the decay in PL intensity by:

$$I \approx I_0 e^{-t/\tau}$$
(Eq. 7)

13

where I_0 is the initial intensity while I is the instantaneous intensity at time t.

E.   LUMINESCENCE IN SEMICONDUCTORS

Luminescence in semiconductors arises when the recombination process between an electron and a hole results in the emission of a photon, releasing energy concurrently (Figure 5). As explained earlier, an excited electron, usually created through the absorption of incident photon energy, resides in the conduction band. Eventually, it will meet with a hole and recombine with it, making a transition from its higher energy state into the lower, but more stable, valence state. The recombination affords the electron a means to liberate its extra energy in the form of a photon emission. Hence, luminescence can be observed. The energy of the emitted photon is approximately equal to the band-gap energy of the semiconductor and the photon wavelength can be found using the following equation:

$$E_g = \frac{1.24}{\lambda} \qquad \text{(Eq. 8)}$$

where E_g is the band-gap energy (in eV), and the λ is the wavelength (in μm).
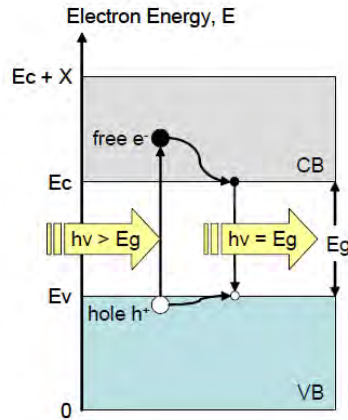

Figure 5.   Photon Absorption and Recombination (From [9])

Each semiconductor material is uniquely characterized by its band-gap energy. Therefore, it is possible to determine the material of a semiconductor by

14

using spectroscopy to analyze the wavelength of the emitted light. The band-gap energy for semiconductors is typically in the range of 0.1 eV to 5 eV.

F.   MULTI-JUNCTION SOLAR CELLS

A solar cell works by converting energy from the sun into usable electricity. When the solar cell is exposed to sunlight, the semiconductor material in the device absorbs energy from the solar radiation. This energy is used to create charge carriers, which are free to flow within the solar cell. Due to the p-n junctions, there is a built-in electric field, which causes the charge carriers to move in a particular direction, thereby creating an electric current. By placing metal contacts at the top and bottom of the solar cell, the current is allowed to flow out of the device for use externally [10].

Energy from the sun consists of photons with a multitude of wavelengths corresponding to the electromagnetic solar spectrum. A solar cell, no matter how efficient, can only work to convert a portion of the sun's energy. The sole factor governing the energy that can be absorbed is the material's band-gap characteristic. In the case of a single-junction solar cell, there is only one band-gap threshold. Photons of energy lower than the band-gap threshold pass through the solar cell without being absorbed, since they have insufficient energy to excite the electrons into the conduction band. For photons with energy higher than the threshold, a portion of the energy is used for the electron to overcome the band-gap and cross to the conduction band, while any excess energy is converted to heat and is dissipated throughout the bulk material. This is unfavorable as it increases the lattice vibration in the semiconductor, leading to shorter lifetime of the charge carriers and therefore, shorter diffusion length. This loss of energy also limits the overall efficiency of the device.

To absorb more photons of different energies and improve the conversion efficiency, multi-junction solar cells are designed. This is achieved by stacking various types of solar cells into a single device. Each cell has a distinct band-gap energy and is thus tuned to absorb photons with energy greater than a specific cut-off wavelength. In general, the solar cells are stacked in decreasing

order of band-gap threshold. The top cell will be able to absorb photons with the highest energies, while the lower energy photons will pass through and be subsequently absorbed by the lower cells, each with a lower band-gap threshold than the one before (Figure 6). Together, the multi-junction cell can now absorb more of the solar radiation while, at the same time, minimizing energy which is lost as heat [11]. Ideally, a multi-junction solar will be made up of hundreds of layers, each able to absorb a certain part of the electromagnetic spectrum. However, due to technological limitations, current multi-junction solar cells are designed with no more than just a few layers (triple-junction solar cell is the most common type at the time of writing) [12].
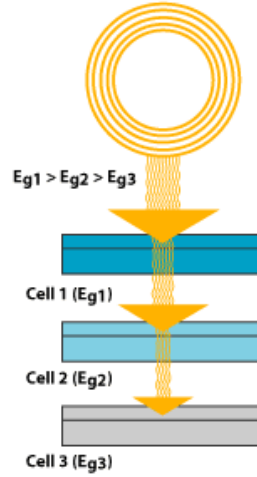
Figure 6.   Schematic of a Triple-Junction Solar Cell. The Top Cell Absorbs Photons with the Highest Energy, E_{g1}, while the Subsequent Cells Absorb Photons with the Lower Energies, E_{g2} and E_{g3} (From [12])

$In_{0.5}Ga_{0.5}P$ is a III – V ternary semiconductor made up of the elements indium, gallium and phosphorous. It is often used as the top layer in the fabrication of multi-junction solar cells due to its large band-gap characteristic and its ability to be grown lattice-matched to Gallium Arsenide (GaAs). It has a near-perfect lattice match with GaAs (lattice mismatch is generally at about 0.2%

[13]), another preferred semiconductor for solar cell manufacturing. This enables InGaP to be easily grown on GaAs, and the two are commonly used as tandem solar cells.

THIS PAGE INTENTIONALLY LEFT BLANK

III.   TRANSPORT IMAGING

A.   DIRECT IMAGING OF FREE CARRIER DIFFUSION

Transport imaging is an optical imaging technique that seeks to directly measure the diffusion length of minority carriers by imaging the spatial dependence of recombination luminescence of a material. In this technique, an external source will be used to locally excite the material, creating electron-hole pairs. This generates a carrier gradient at the point of excitation and induces the subsequent diffusion of the minority charge carriers. The image of the luminescence distribution, as a result of the radiative recombination of the carriers as they diffuse, is captured using a charge-coupled device (CCD) camera. Unlike the traditional cathodoluminescence (CL) method, the spatial information of the luminescence distribution is retained [14], allowing for the extraction of the diffusion length and the subsequent calculation of the minority charge carrier mobility.

One advantage of transport imaging over the conventional Haynes-Shockley technique is that contacts do not need to be added to the sample in order to induce an electric field necessary to move the minority charge carriers. This is also the advantage over electron-beam-induced current (EBIC) techniques, which require a rectifying contact to collect electron-beam induced charge. In addition, it can be performed with much higher spatial resolution.

B.   LABORATORY EQUIPMENT

1.   SEM

In this experiment, the external excitation source will consist of an electron beam generated in a SEM. The SEM used is the JEOL 840A model and it is fitted with a modified stage from Oxford Instruments to allow the intake of helium gas for the cooling of the sample stage (Figure 7). This modification enables measurement of the sample to be conducted at a range of temperatures—from

room temperature of 300K to a low temperature of 5K. There is also an optical microscope attached to collect the luminescence from the samples.
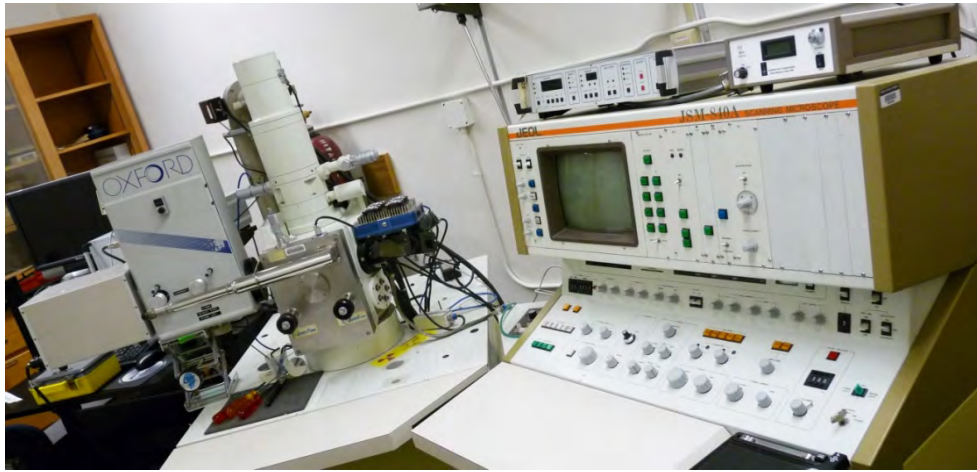
Figure 7.   JEOL 840A SEM with Modified Variable Temperature Stage

The SEM can be adjusted to operate in three separate modes—spot mode, line mode and picture mode (Figure 8). In spot mode, the electron beam is held fixed at a specified spot, allowing charge carriers to be generated from that quasi-point source. In line mode, the electron beam is scanned along a "line" and charges are generated along the beam path. In picture mode, the beam scans over a specified region, allowing an area "picture" of the material imaged.

a

b

c
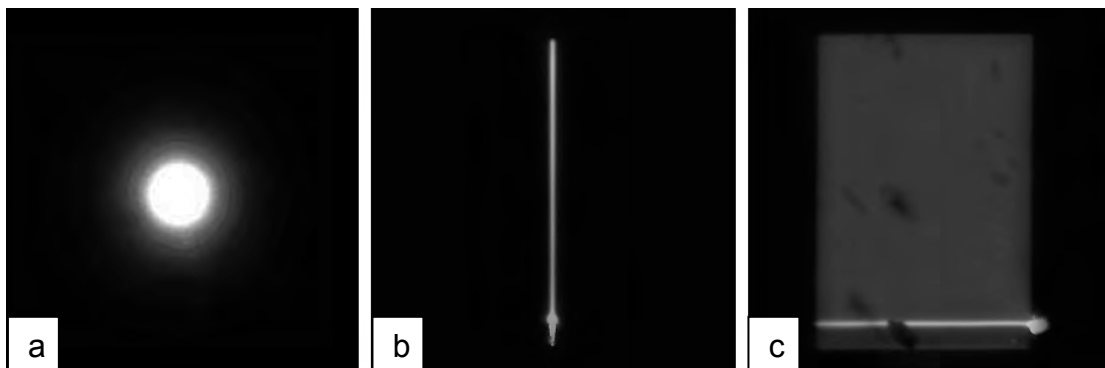
Figure 8.   SEM Imaging Modes: (a) Spot Mode, (b) Line Mode and (c) Picture Mode

2. Optical Detector

The optical detector connected to the optical microscope for luminescence imaging is an Apogee CCD camera (Figure 9). It has a 2184 x 1472 pixel array. When coupled to our optical microscope, the resolution is 0.4 µm per pixel. In an unfiltered setting, the camera can efficiently collect data for light of wavelengths in the range of 400 to 1100 nm. To minimize the effect of thermal noise, the camera can also be cooled to a temperature of -20 °C prior to operation.

Figure 9.   Apogee CCD Camera

Figure 10 shows the overall operation of transport imaging measurement system as well as a schematic of the components used.
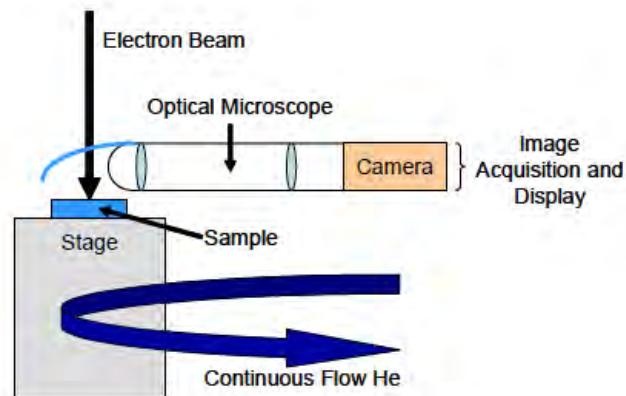
Figure 10.   Transport Imaging Operation and Components (After [15])

C.   DATA COLLECTION

For transport imaging, both the spot mode and line mode can be used. However, the line mode was predominantly used for these experiments due to the relative ease of the extraction of diffusion length data as compared to that when spot mode is used. The reason for this is further discussed in Section D.

For each sample, two separate images—the "luminescence" image and the "dark" image—were taken (Figure 11). The first is the luminescence image, which shows the steady state luminescence distribution of the sample when exposed to the SEM's electron beam. The second is the dark image of the sample when the electron beam has been turned off or blocked. This image, though appearing totally black to the naked eye, actually captures the background CCD response due to thermal generation in the detector and any background light in the chamber. During data processing, the luminescence count from the dark image is subtracted from the count of the luminescence image to acquire a more accurate luminescence distribution, which is due solely to the material itself. To obtain a higher level of accuracy, both images are taken over the same region of the sample and exposed for the same duration of time.
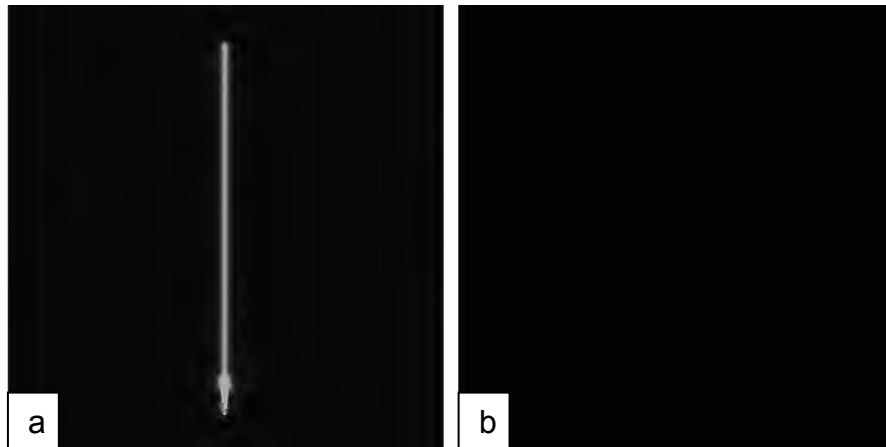
Figure 11.   Data Collection for a 10s Exposure: (a) the Luminescence Image and (b) the Dark Image [712 pixels (285 μm) x 712 pixels (285 μm)]

Another important factor to ensure the proper capturing of the luminescence distribution is to have a good signal-to-noise ratio (SNR). For the experiment, the camera is exposed to the sample for a period of time (which will vary between samples due to their different luminescence intensity) such that the peak intensity reaches a count of approximately 25,000 or higher. With the background count at about 200, a good SNR of close to 50dB can be achieved. Figure 12 shows the horizontal intensity profile of a sample luminescence image in line mode.
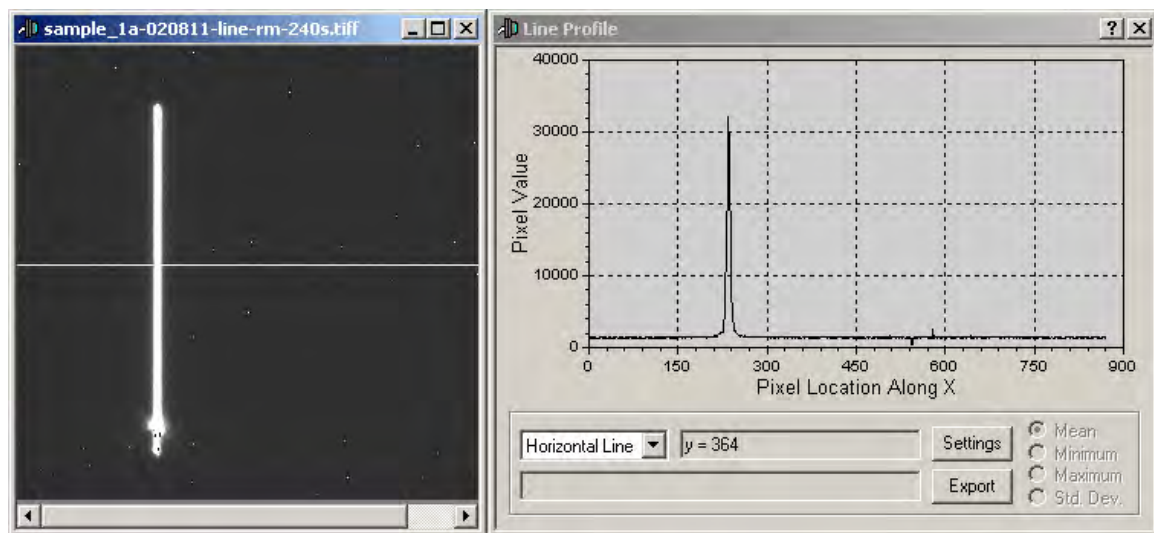
Figure 12. Intensity Profile of a Luminescence Image (Extracted Perpendicular to the Excitation Line)

D. DIFFUSION LENGTH EXTRACTION

1. 2D Diffusion Case

The extraction method for the diffusion length depends on the imaging mode with which the sample was taken. In the case of a spot mode, the minority charge carriers are allowed to diffuse from a fixed generation point. Assuming that the sample is a thin layer and that the diffusion is thus confined to a plane, the charge carriers will follow a two-dimensional (2D) pattern of diffusion (Figure 13).
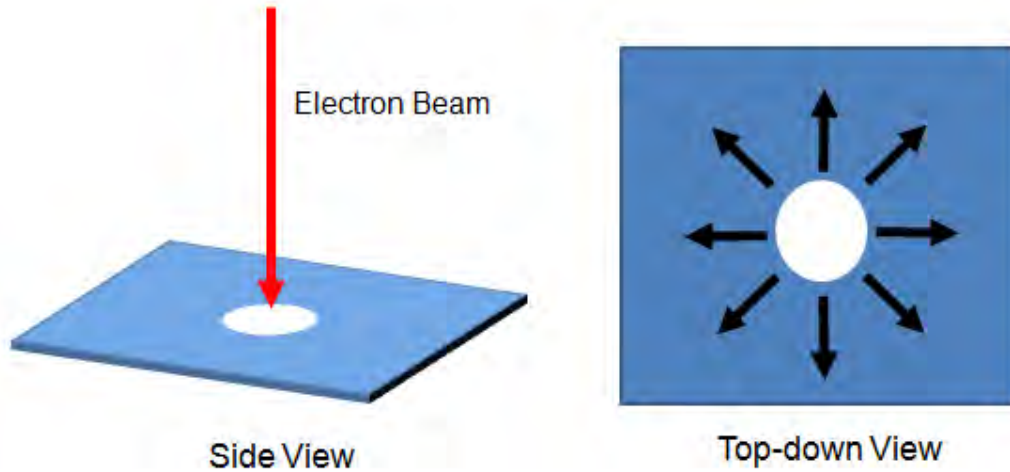
Figure 13. 2D Diffusion of Charge Carriers

This diffusion can be modeled as a zeroth-order modified Bessel function of the second kind [14] and the continuity equation involving the minority carrier distribution and related recombination luminescence, I, can be expressed as:

$$0 = D\nabla^2 I - \frac{1}{\tau}I + S(r) \qquad \text{(Eq. 9)}$$

where D is the minority charge carrier diffusivity, τ is the minority charge carrier lifetime and is $S(r)$ the source function.

The luminescence, I, resulting from a point source, $S(r)$, can then be defined by solving the differential equation given in Equation 9 and subsequently approximated by:

$$I(r) = \frac{g}{2\pi D} K_0(r/L_{diff}) \qquad \text{(Eq. 10)}$$

where g is the amplitude of the source, K_0 is the zeroth-order modified Bessel function of the second kind, r is the radius of diffusion and L_{diff} is the diffusion length. The diffusion length, L_{diff}, is determined from a least squares analysis for variations in L_{diff}.

2.   1D Diffusion Case

In the case of a line mode, the electron beam scans up and down the sample along a straight path, causing the charge carriers to diffuse from a line source.   Since only the exitance condition is different for the charge carriers diffusing at either ends of the line, the charge carriers in the middle (as depicted by the yellow box in Figure 14) can be considered to be following a one-dimensional (1D) diffusion model.

Electron Beam

Side View

Top-down View
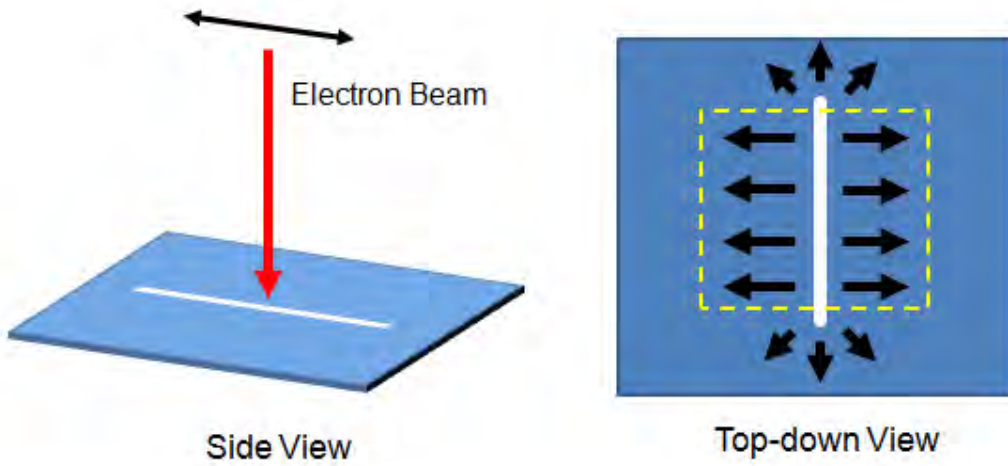
Figure 14.   1D Diffusion of Charge Carriers

The 1D minority charge distribution falls off exponentially as a function of the distance and the luminescence, I , can be expressed as:

$$I = I_0 e^{\frac{-x}{L_{diff}}}$$

(Eq. 11)

where I_0 is the peak intensity, x is the distance of diffusion from the line and L_{diff} is the diffusion length.

After normalizing luminescence, the diffusion length can be calculated by:

$$L_{diff} = -\frac{\Delta x}{\Delta \ln I_N}$$ (Eq. 12)

where I_N is the normalized luminescence (i.e. $I_N = \frac{I - I_{min}}{I_0 - I_{min}}$).

If the semi-logarithmic graph of the normalized luminescence intensity, I_N, against position, x, is plotted, then the diffusion length, L_{diff}, can be directly determined as the inverse slope value of the graph (Figure 15). This is known as the 1/slope technique.
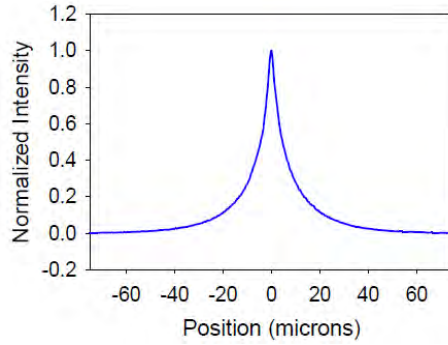
(a) Plot of Normalized Intensity against Position
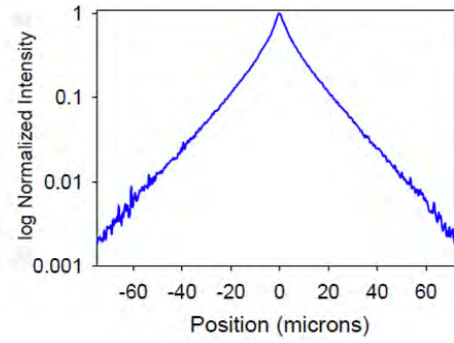
(b) Semi-Logarithmic Plot of Normalized Intensity against Position
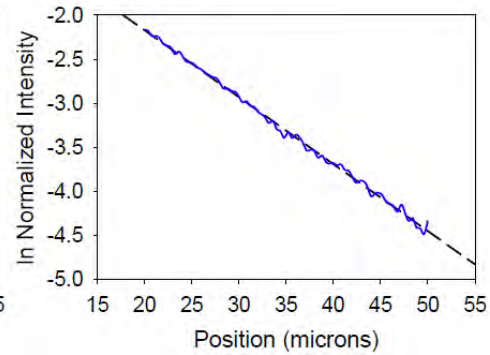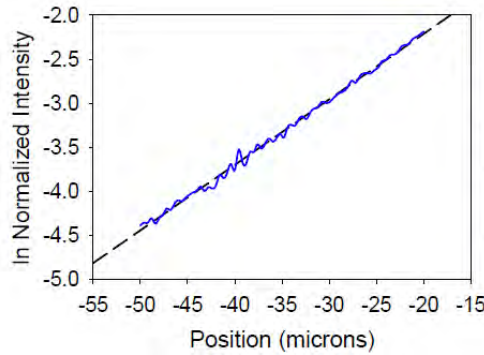
(c) Linear Regression Lines for (Left and Right) Slope Extraction

Figure 15. 1/Slope Technique (From [15])

IV. EXPERIMENTAL RESULTS OF MEASURING MINORITY CARRIER DIFFUSION LENGTH IN INDIUM GALLIUM PHOSPHIDE

A. SAMPLES

For this experiment, four sets of InGaP heterostructures were provided through collaboration with other researchers in the solar cell field. Three of the sets had p-type InGaP material with two different doping levels while the last set had n-type InGaP material. Within each set of the heterostructures, there were three samples with varying thicknesses for the InGaP layer at 0.3 μm, 0.5 μm, and 1.0 μm, respectively. Therefore, there were a total of twelve heterostructure cells for diffusion length measurement.

1. Set 01: p-type InGaP (Higher Doping)

Set 01 samples consisted of $Al_{0.25}Ga_{0.25}In_{0.5}P$ barrier layers with a middle p-type $In_{0.5}Ga_{0.5}P$ layer with a doping level of 1×10^{17} cm^{-3} (Figure 16). The three samples within this set had different thicknesses of 0.3 μm, 0.5 μm, and 1.0 μm for the InGaP layer. These samples will be labeled as sample 1A, sample 1B, and sample 1C, respectively.
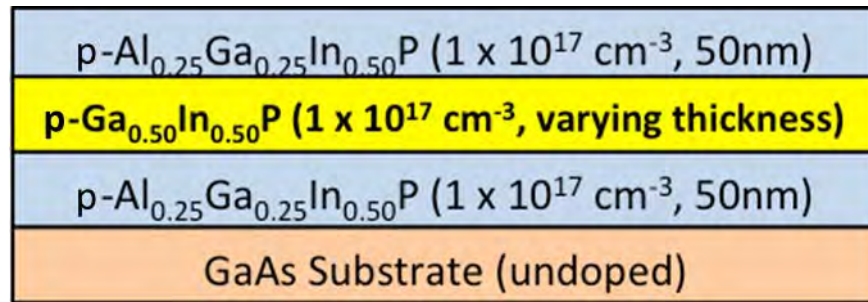
Figure 16. Set 01 Samples with 1×10^{17} cm^{-3} P-Type InGaP Layer

2. Set 02: p-type InGaP (Lower Doping)

Set 02 samples consisted of $Al_{0.25}Ga_{0.25}In_{0.5}P$ barrier layers with a middle p-type $In_{0.5}Ga_{0.5}P$ layer with a doping level of 5×10^{16} cm^{-3} (Figure 17). The

three samples within this set had different thicknesses of 0.3 µm, 0.5 µm, and 1.0 µm for the InGaP layer. These samples will be labeled as sample 2A, sample 2B, and sample 2C, respectively.

Figure 17. Set 02 Samples with 5 x 10^{16} cm^{-3} P-Type InGaP Layer

3.   Set 03: p-type InGaP (Lower Doping)

Set 03 samples consisted of Al$_{0.25}$Ga$_{0.25}$In$_{0.5}$P barrier layers interfaced with a middle p-type In$_{0.5}$Ga$_{0.5}$P layer with a doping level of 5 x 10^{16} cm^{-3} (Figure 18). This doping level was the same as that of those in Set 02. The three samples within this set had different thicknesses of 0.3 µm, 0.5 µm, and 1.0 µm for the InGaP layer. These samples will be labeled as sample 3A, sample 3B, and sample 3C, respectively.

Figure 18. Set 03 Samples with 5 x 10^{16} cm^{-3} P-Type InGaP Layer

4. Set 04: n-type InGaP

Set 04 samples were the only n-type $In_{0.5}Ga_{0.5}P$ heterostructures, with the highest doping level of 8 x 10^{17} cm^{-3} (Figure 19). The three samples within this set had different thicknesses of 0.3 μm, 0.5μm, and 1.0 μm each, and will be labeled as sample 4A, sample 4B, and sample 4C, respectively.

| n-Al$_{0.50}$In$_{0.50}$P (1 x 10^{17} cm^{-3}, 50nm) |
| n-Ga$_{0.50}$In$_{0.50}$P (8 x 10^{17} cm^{-3}, varying thickness) |
| n-Al$_{0.50}$In$_{0.50}$P (1 x 10^{17} cm^{-3}, 200nm) |
| GaAs Substrate (undoped) |
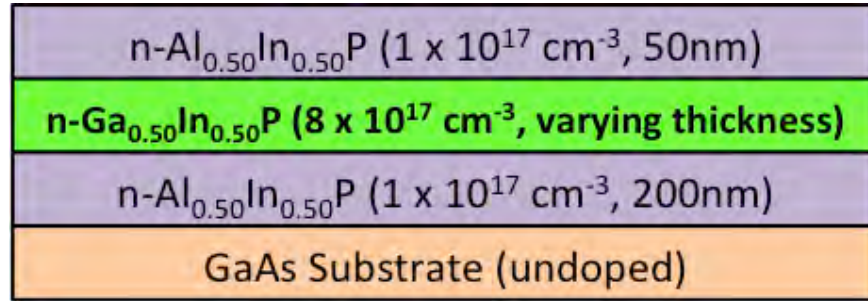
Figure 19. Set 04 Samples with 8 x 10^{17} cm^{-3} N-Type InGaP Layer

A summary of the twelve samples is given in Table 1.

Set #	Type	Sample Name	Thickness (μm)
1	p-InGaP (Higher doping – 1 x 10^{17} cm^{-3})	1A	0.3
		1B	0.5
		1C	1.0
2	p-InGaP (Lower doping – 5 x 10^{16} cm$^{-3)}$	2A	0.3
		2B	0.5
		2C	1.0
3	p-InGaP (Lower doping – 5 x 10^{16} cm^{-3})	3A	0.3
		3B	0.5
		3C	1.0
4	n-InGaP (Doping – 8 x 10^{17} cm^{-3})	4A	0.3
		4B	0.5
		4C	1.0

Table 1. InGaP Heterostructure Sample Sets

B.   CATHODOLUMINESCENCE SPECTRA OF SAMPLES

Prior to the transport imaging experiment, CL spectroscopy was performed to determine the radiative spectrum of the samples. Figure 20 shows the room temperature CL spectra results of the 1 µm thick samples from each set. From the graph, it is observed that photoluminescence occurred at only one peak wavelength for each of the sample sets. These luminescence peaked at a wavelength of approximately 650 nm, which corresponds to the InGaP bandgap of about 1.9 eV [16]. The slight shift in wavelength is likely a result of the different doping levels of the sample sets. This ensures that the photoluminescence to be used for the transport imaging originated purely from the InGaP layer and that there was no higher energy interference from the barrier layers or the substrate itself.
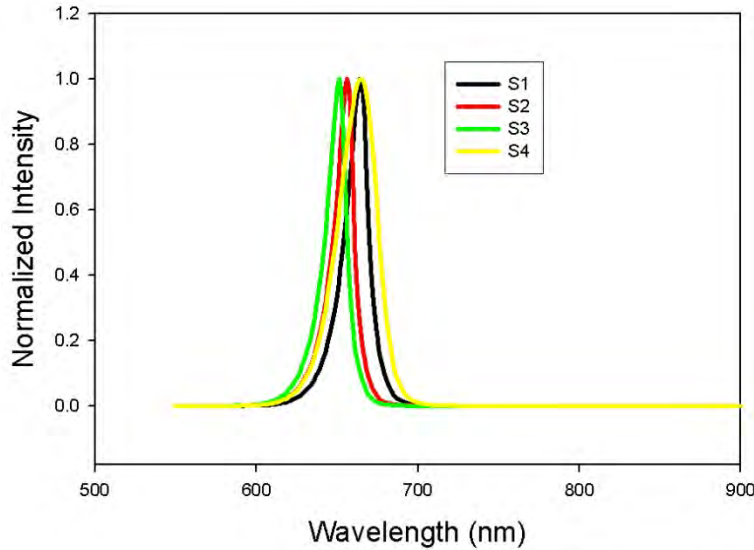
Figure 20.   CL Spectra of 1 µm Thick Samples of Each Set at 300K

C.   EXPERIMENTAL RESULTS

The main objective of the experiment was to apply the transport imaging technique on each of the twelve samples in order to determine their minority carrier diffusion lengths. The mobility values could therefore be subsequently

determined since independent TRPL data were available.   For all the experiments on the InGaP samples, the SEM was set with the experimental configuration as given in Table 2.

SETTING	VALUE
Electron Beam Energy	10 keV
Probe Current	3×10^{-11} A
Magnification	x 500

Table 2.   SEM Operating Parameters for InGaP Measurements

For each sample, two sets of measurements were taken—one at room temperature and the other at low temperature (5K).

1.   Room Temperature Measurements

Figure 21 shows the luminescence distributions of all the samples from Set 01 to Set 04 taken at room temperature (i.e., 300k). These luminescence distributions were obtained by subtracting the ambient light and detector thermal noise (captured in the dark images) from the recombination luminescence of the samples (captured in the luminescence images). The distributions were then plotted as semi-logarithmic graphs of the normalized luminescence intensity, I_N, plotted against the position, x.

(a) Set 01

(b) Set 02

32
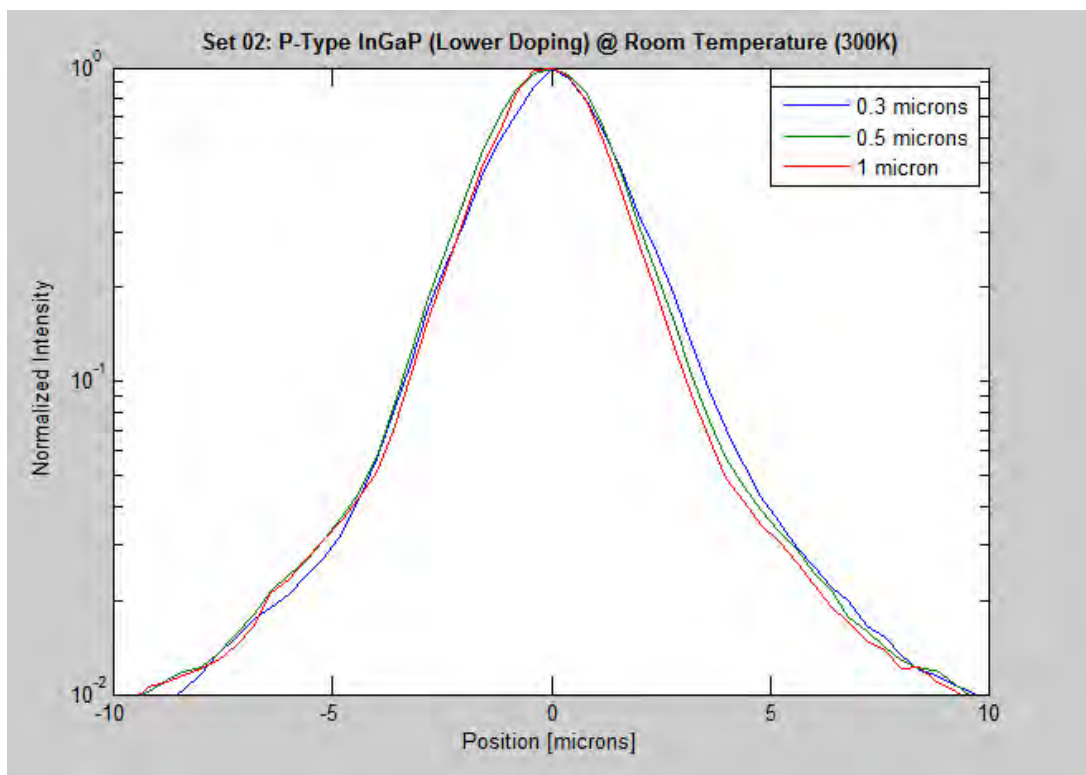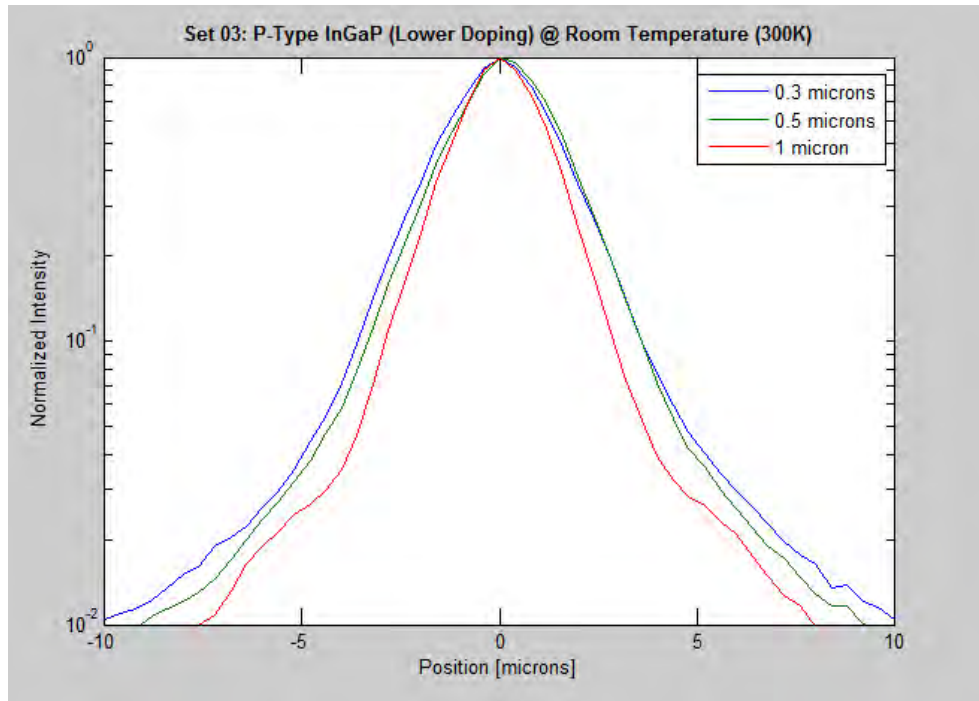
(c) Set 03
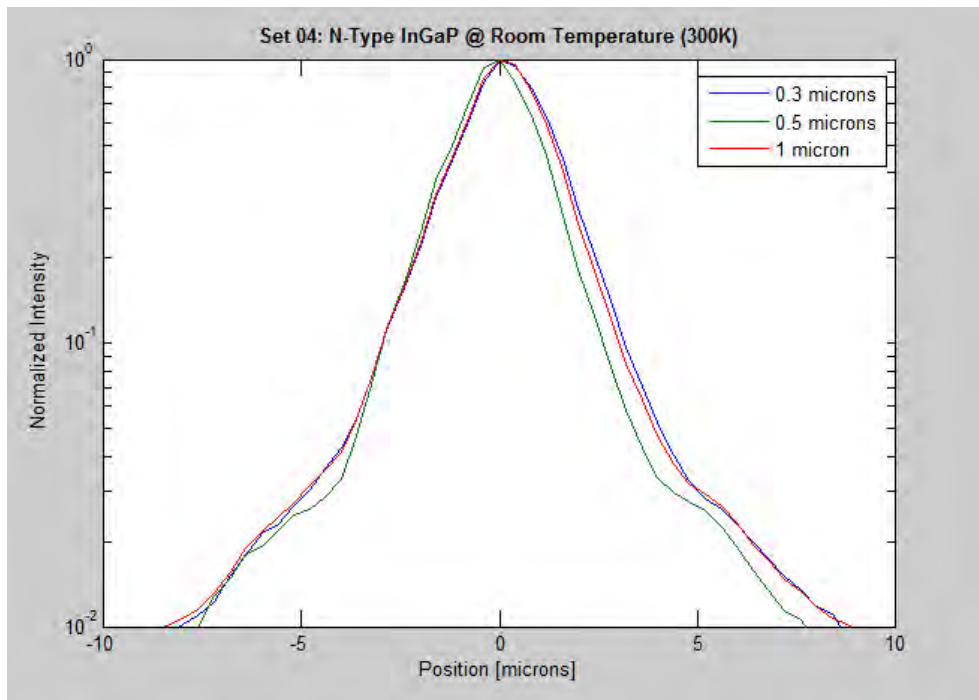
(d) Set 04

Figure 21.   Normalized Luminescence Intensity as a Function of Position at 300K
for Samples in Sets 01 to 04

2. Low Temperature Measurements

Figure 22 shows the luminescence distributions of all the samples from Set 01 to Set 04 taken at 5K.
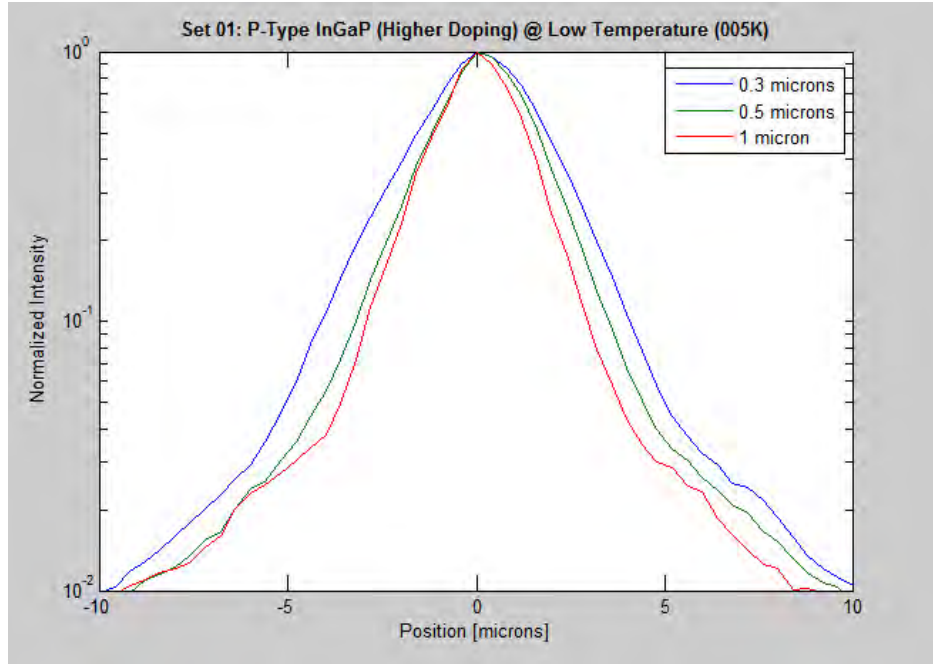
(a) Set 01
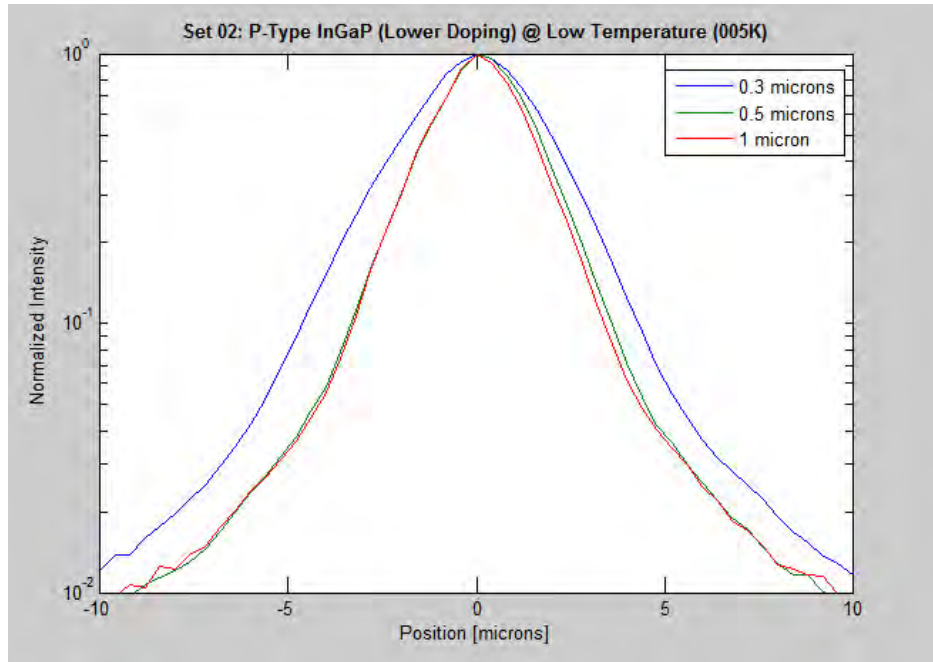
(b) Set 02
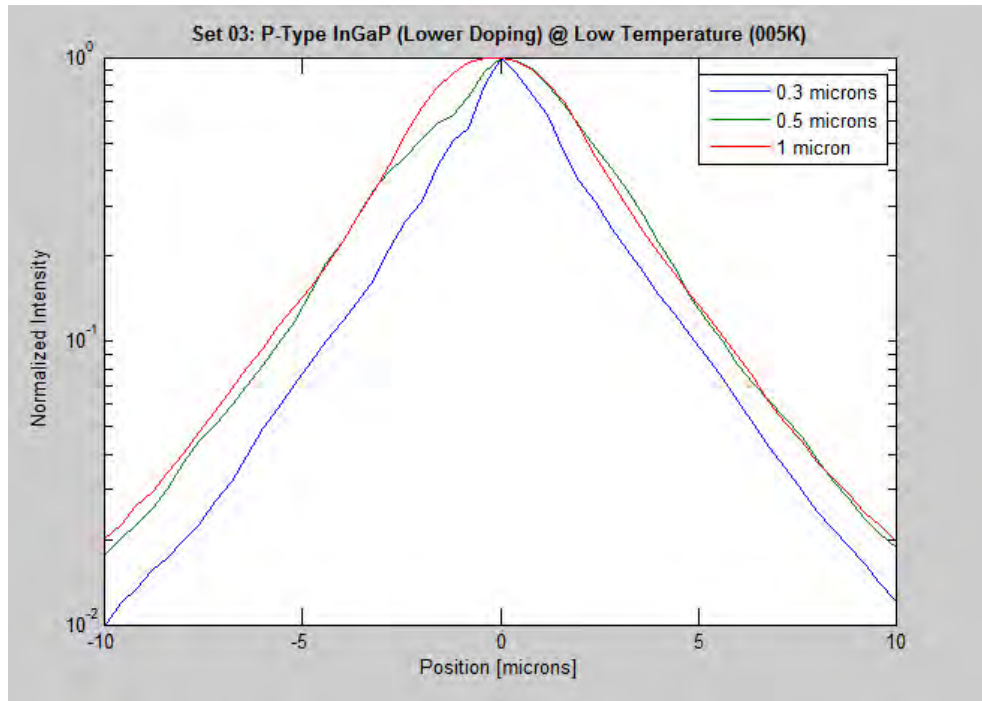
(c) Set 03
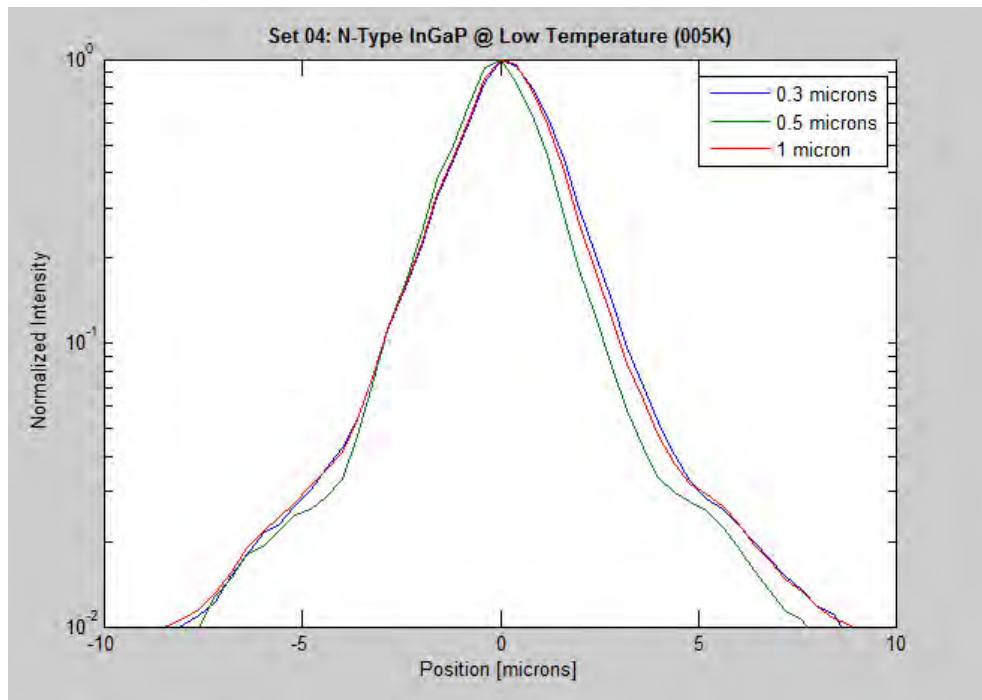
(d) Set 04

Figure 22.   Normalized Luminescence Intensity as a Function of Position at 5K
for Samples in Sets 01 to 04

3. Results of Diffusion Length Extraction

From the luminescence distribution of the samples, the gradient of the distribution slopes could be obtained and the diffusion length was calculated as the inverse of the slope gradient, using the 1/slope technique.

Figure 23 illustrates how line-fitting was performed on the diffusion distributions for four of the samples (two at 300K and two at 5K) in order to determine the gradient of the slopes. In general, the position data (x-axis) used for the line-fitting was approximately in the range of 1.0 μm to 3.6 μm, though the actual data used varied for each set depending on the distribution. Interestingly, the distribution of Set 3 samples spread out significantly at low temperature, allowing a wider range of data to be used for the line-fitting (Figure 23d).
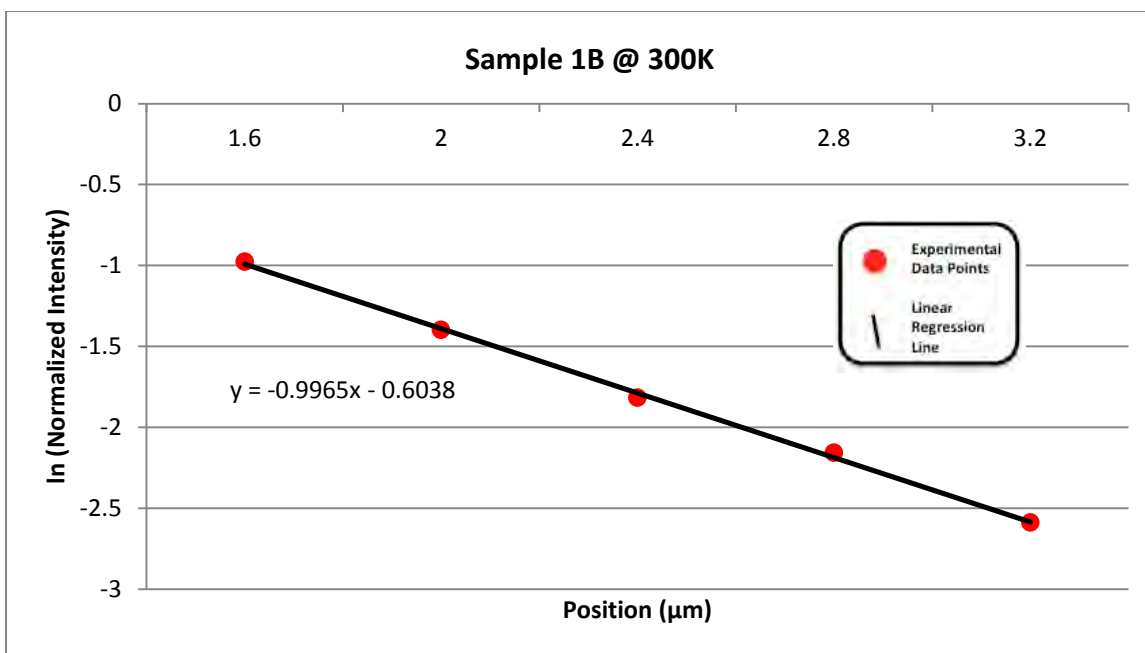
(a)   Set 1B (300K)
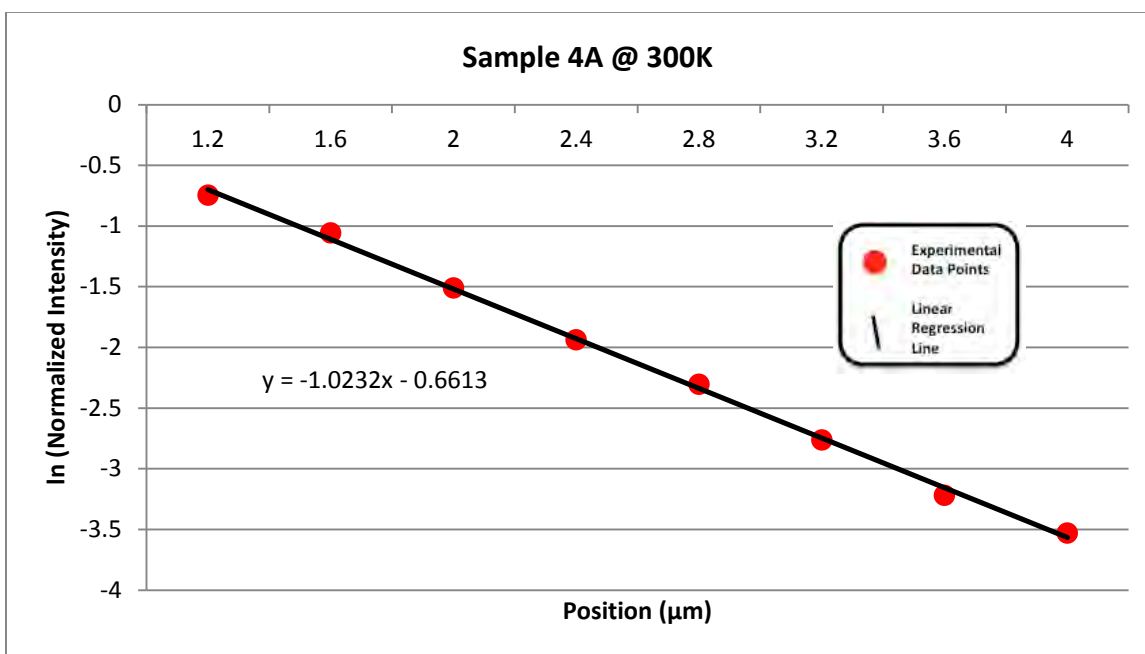
(b)   Set 4A (300K)
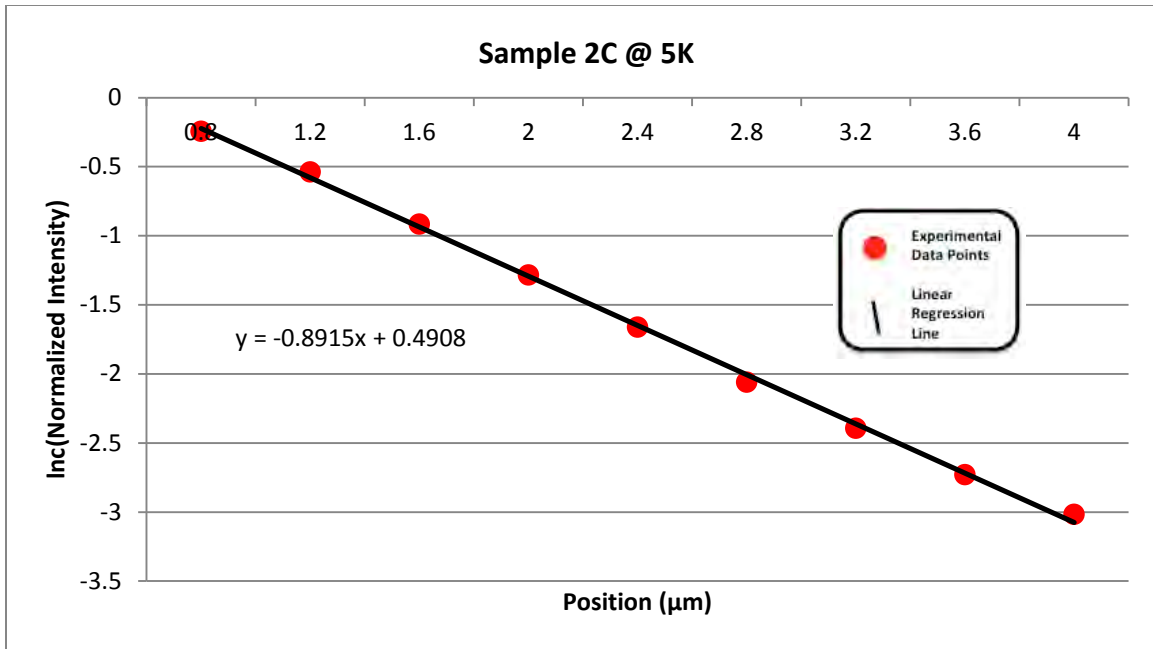
(c)   Set 2C (5K)
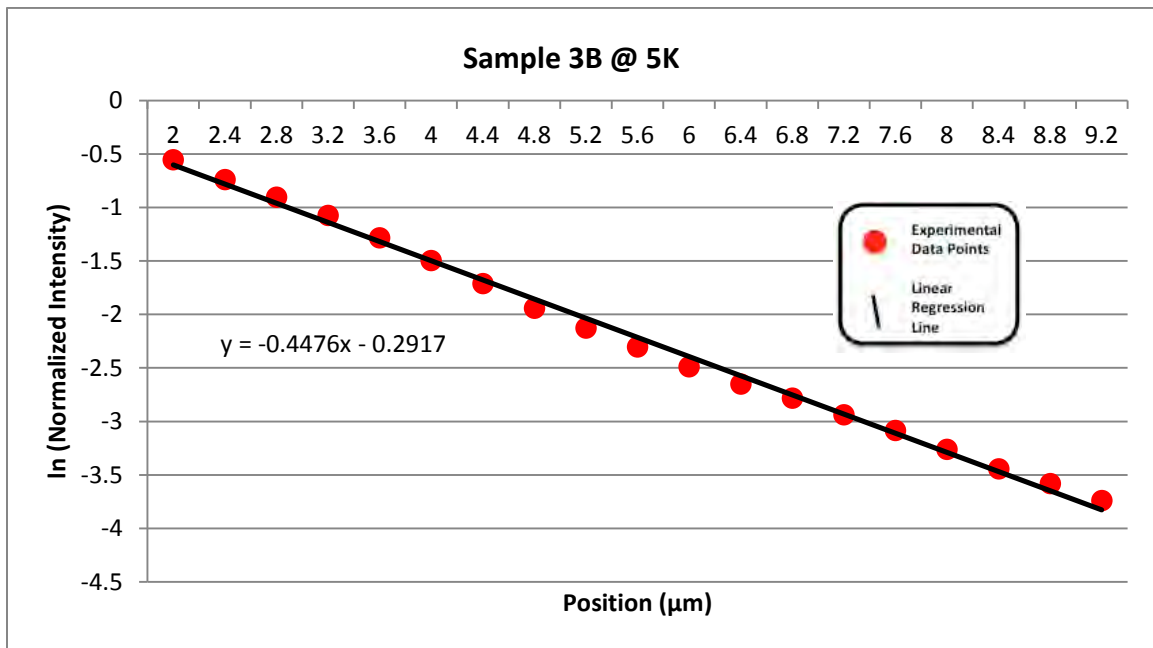
(d)   Set 3B (5K)

Figure 23.   Plots of Ln (Normalized Intensity) as a Function of Position for
Gradient Extraction for InGaP Samples

Table 3.   shows the calculation of the diffusion lengths using the gradient of the slopes obtained via the earlier line-fitting process.

Sample	Temperature (K)		Gradient (μm^{-1})	Diffusion Length (μm)
1B	300		-0.997	1.00
4A			-1.023	0.98
2C	5		-0.892	1.12
3B			-0.448	2.23

Table 3.   Calculation of Diffusion Lengths

The summary of the diffusion length values for all the twelve samples is tabulated in Table 4.

Set #	Type	Sample	Thickness (μm)		Diffusion Length @ 300K (μm)	Diffusion Length @ 5K (μm)
1	p-InGaP (Higher doping – 1×10^{17} cm^{-3})	1A	0.3		1.11	1.24
		1B	0.5		1.00	1.18
		1C	1.0		0.99	1.13
2	p-InGaP (Lower doping – 5×10^{16} cm^{-3})	2A	0.3		1.17	1.28
		2B	0.5		1.12	1.15
		2C	1.0		1.06	1.12
3	p-InGaP (Lower doping – 5×10^{16} cm^{-3})	3A	0.3		1.60	2.15
		3B	0.5		1.30	2.23
		3C	1.0		1.24	2.18
4	n-InGaP (Doping – 8×10^{17} cm^{-3})	4A	0.3		0.98	0.98
		4B	0.5		0.95	1.00
		4C	1.0		0.94	0.95

Table 4.   InGaP Sample Diffusion Length Results

D.   ANALYSIS OF RESULTS

1.   Material Type

The measurements clearly showed that Set 01 to Set 03 samples, which were p-type materials, had broader luminescence distributions than Set 04 samples, which were n-type materials. Figure 24 shows one such comparison of the distributions for the set of samples with 0.3 µm InGaP layers at room temperature. This indicated that the p-type materials had longer diffusion lengths than the n-type materials. In p-type materials, the minority charge carriers were electrons while the minority charge carriers for n-type materials were holes. Literature values for majority carrier mobility have indicated that the mobility for electrons is much higher than that of holes [17], which is likely to result in longer diffusion lengths when the lifetimes are comparable.   Therefore, it is within expectation for the p-type materials to have longer diffusion lengths than the n-type materials.
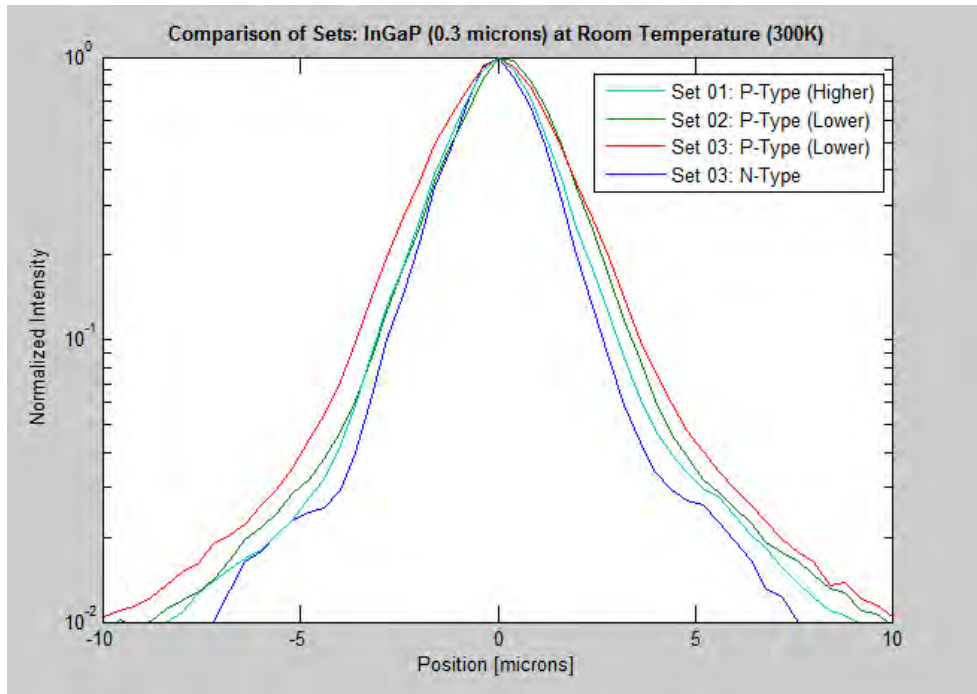
Figure 24. Comparison of Luminescence Distributions of Samples with 0.3 µm InGaP Layer at 300K

2.   Doping Level

By comparing the p-type materials (i.e., Set 01 to Set 03), the experimental results showed that samples in Set 02 and Set 03, with a lower doping level, had longer diffusion lengths than those in Set 01, which were higher-doped. This was also shown by the broader luminescence distributions of the higher-doped samples in Figure 24.

In semiconductors, the doping level has an influence on the diffusivity of the minority charge carriers. When dopants are introduced into a material, they are generally ionized at room temperature, by either accepting or donating electrons to the material. In either case, the ions, being charge centers, act as scattering sites. When the minority charge carriers diffuse through the material, they can be scattered or deflected from their original path by the Coulomb force exerted by these dopant ions. Therefore, as the doping level increases, which implies a higher dopant concentration, the probability of the minority charge carriers encountering scattering or deflection is now greater. This, in turn, lowers the diffusivity of the charge carriers, resulting in shorter diffusion lengths.

3.   Thickness

From the graphs (Figure 21 for room temperature measurements and Figure 22 for low temperature measurements), it could be seen that in general, the distribution narrowed with increasing thickness for each set. The difference in the distribution width was very clearly demonstrated in the case of Set 02 and Set 03 samples, though it was not so obvious in the case of Set 01 and Set 04 samples. Since a narrower distribution has steeper slopes, the slope gradient will have a higher value when compared with that of broader distributions. This implies that the diffusion length, which was calculated as the inverse of the slope gradient, would be shortest for the sample with the highest thickness within each set.

A possible explanation for this is that as the thickness increases, the minority charge carriers are less confined to 1D or 2D diffusion and start to

experience diffusion in the depth too, resulting in 3D diffusion. As such, the charge carriers diffuse in a volumetric manner and the apparent diffusion length decreases, since the 2D model was applied in all cases.

4.   Temperature

A comparison of the luminescence distributions of sample 1C at various temperatures (i.e., from 300K to 5K) is given in Figure 25. From the graph, it could be observed that as temperature dropped, the distribution started to widen, thereby giving longer diffusion lengths for the same sample. This observation was the same for the other sample sets.

The diffusivity of minority charge carriers is also influenced by temperature. Due to thermal energy, the atoms within a lattice are not at rest, but constantly vibrating about their fixed positions. These quantized vibrational states are known as phonons. As the charge carriers travel through the material, they will eventually interact with such a phonon and be deflected from their original paths. Thus, the vibration causes scattering of charge carriers. As temperature increases, the atoms gain more thermal energy and the population of phonons increases as well. This causes more scattering of the charge carriers, leading to lower carrier mobility at higher temperature.

The actual change in mobility is also affected by the fact that these materials were ternary alloys. In this case, alloy disorder scattering plays a significant role, weakening the effect of temperature, compared to a binary material, such as GaAs or Indium Phosphide (InP).
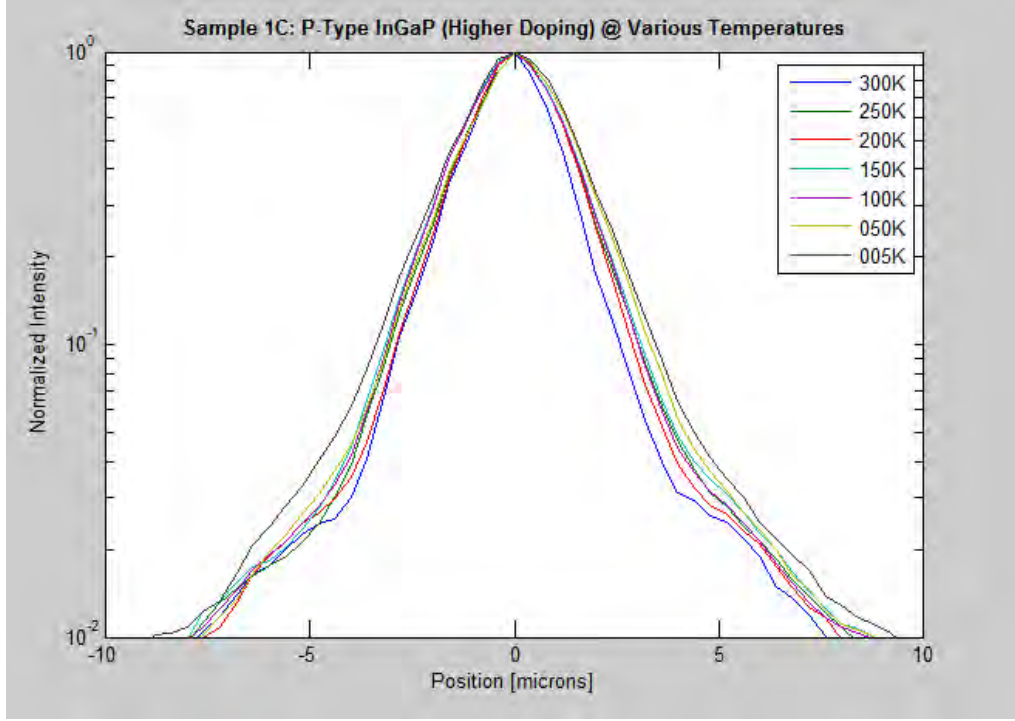
Figure 25.   Comparison of Sample 1C Luminescence Distributions at Various Temperatures

E.   RESULTS OF MOBILITY VALUE CALCULATION

The next objective, having obtained the diffusion lengths, was to determine the mobility values of the minority charge carriers in the samples. The sample providers had earlier acquired the minority charge carrier lifetime data of their samples by means of TRPL. Using the diffusion length data, together with the lifetime data set, the minority charge carrier mobility, μ, could be easily calculated using the following equation:

$$\mu = \frac{L_{diff}^{2} e}{\tau k T}$$

Eq. (13)

where L_{diff} is the diffusion length, e is the electron charge, τ is the minority charge carrier lifetime, k is the Boltzmann's constant and T is the temperature. Note that this is just a rearrangement of Equation 3. It should be highlighted that the lifetime data were obtained at room temperature settings and, therefore,

43

could not be used to evaluate the mobility values of the samples at low temperature. The results—for the room temperature measurements only—are summarized in Table 5.

Set #	Type	Sample	Thickness (μm)		Diffusion Length @ 300K (μm)	Lifetime @ 300K (ns)	Mobility @ 300K (cm^{2}V^{-1}s^{-1})
1	p-InGaP (higher doping – 1 x 10^{17} cm^{-3})	1A	0.3		1.11	1.13	421
		1B	0.5		1.00	1.03	375
		1C	1.0		0.99	1.32	287
2	p-InGaP (lower doping – 5 x 10^{16} cm^{-3})	2A	0.3		1.17	1.07	494
		2B	0.5		1.12	0.83	584
		2C	1.0		1.06	0.95	457
3	p-InGaP (lower doping – 5 x 10^{16} cm^{-3})	3A	0.3		1.60	1.36	727
		3B	0.5		1.30	1.37	477
		3C	1.0		1.24	1.55	383
4	n-InGaP (higher doping – 1 x10^{17} cm^{-3})	4A	0.3		0.98	2.28	163
		4B	0.5		0.95	2.07	168
		4C	1.0		0.94	2.11	162

Table 5.   InGaP Minority Charge Carrier Mobility Results

F   OBSERVATIONS

One observation of the TRPL data set was that the minority carrier lifetimes did not follow a specific trend. Normally, one would expect the lifetime values to increase with increasing thickness for samples within each set of the same material type and doping level due to improvement in material quality and a smaller role in surface recombination. However, this was not really observed and, instead, there were many cases where the lifetimes were shorter for the thicker samples. This showed that the fabrication process employed to manufacture these samples might not have been mature yet, resulting in inconsistencies in the material uniformity or defects, which could affect the

transport behavior of the charge carriers. Another possibility was that surface recombination in these samples was very low and the variations in lifetime data represented the experimental error.

Another critical observation from the results was that the hole mobility values extracted from the simple slope analysis appeared to be too high. Though literature data on minority charge carrier mobility is scarce, there is good indication that the norm of such mobility is in the range of 100 to 1000 $cm^2V^{-1}s^{-1}$ for electrons and 10 to 100 $cm^2V^{-1}s^{-1}$ for holes [17]. While the electron carriers presented mobility values of 300 to 700 $cm^2V^{-1}s^{-1}$, which were within the expected range, the experimental results of about 160 $cm^2V^{-1}s^{-1}$ for holes were higher than expected.

One possibility for this phenomenon was that the actual diffusion lengths of the samples were much shorter than those that were derived from the 1/slope technique of the luminescence distribution. Due to the short diffusion lengths, the luminescence distributions seen in the graphs were most likely a convolution of the actual diffusion behavior with the finite size of the SEM's electron beam. Therefore, the diffusion lengths of the samples could not be effectively determined by using the 1/slope technique of this convolved luminescence, since it was also affected by the size of the generation region for the charge carriers.

In earlier work on transport imaging, the samples all had considerably long diffusion lengths, such that the recombination luminescence occurred even when "far away" from the electron beam. This allowed the 1/slope technique to remain effective as the luminescence distribution was dominated by diffusion without major interference from the finite generation region.   For these samples, however, the 1/slope technique failed. To determine the real diffusion lengths, there is now a need to separate the resulting luminescence into its individual components—the diffusion behavior in the samples and the incident electron beam interaction. This will be discussed in the next chapter.

THIS PAGE INTENTIONALLY LEFT BLANK

V.   DECONVOLUTION MODEL FOR OVERCOMING THE FINITE VOLUME GENERATION LIMITATION

A.   EXPERIMENTAL LIMITATION

The results of the charge carrier mobility values presented in the previous chapter were found to be significantly higher than would be expected based on literature values for majority carrier mobility in InGaP, particularly for the minority holes in the n-type samples. One hypothesis was that the minority diffusion lengths of the samples were sufficiently short (0.5 µm to 2.0 µm) to be of the same order of magnitude as the finite charge carrier volume generation region due to the electron beam. As such, when the transport imaging technique was applied, what was captured by the CCD camera was the convolved product of the actual recombination luminescence from the samples with the finite charge carrier volume generation. Therefore, when the charge carrier mobility was calculated without including the effect of the finite size of the source beam, the results deviated significantly.

The volume generation region can be illustrated using a Monte Carlo simulation. CASINO, a simulation program based on the Monte Carlo algorithm, was used to simulate the effect of transport imaging using a 10 keV beam source on a 0.3 µm thick InGaP layer on GaAs (Figure 26). From the graph, the existence of the generation region was clearly depicted and the region even extended to a depth beyond the InGaP material. Laterally, the generation region extended to a width of approximately 0.5 µm. The consequence is that if the diffusion length of the samples were short, the recombination luminescence would become coupled with the effect of the generation volume. This is a limitation that must be addressed in the model for short diffusion length materials.
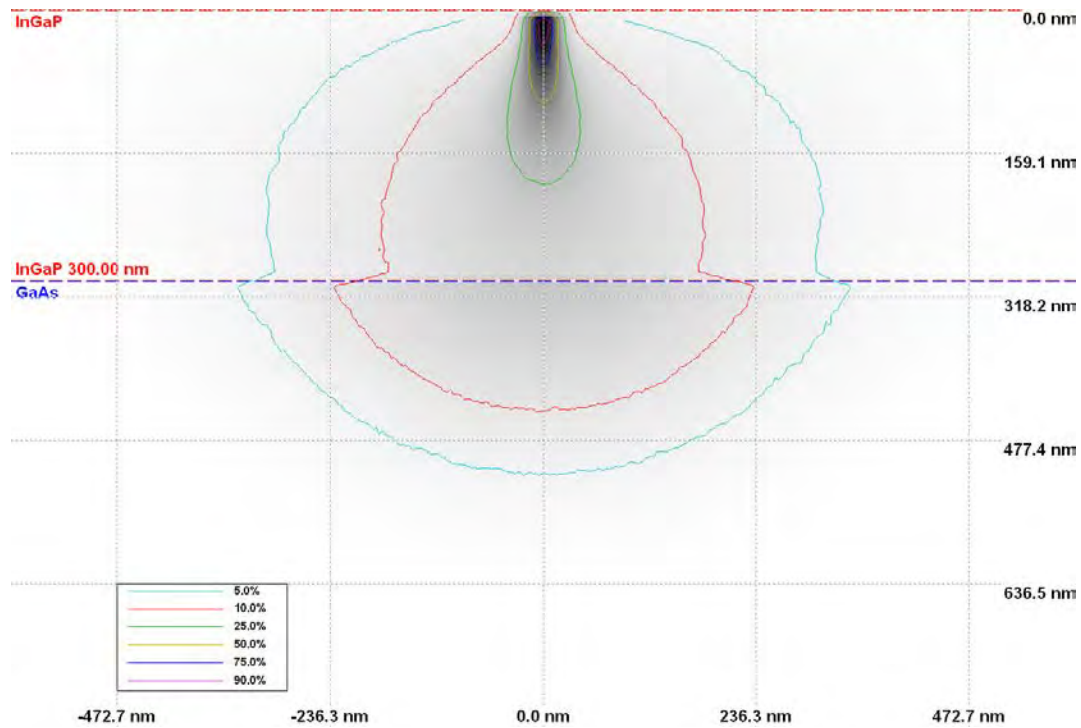
Figure 26. Monte Carlo Simulation Showing Finite Generation Volume. The Image Shows the Energy Distribution in Both Lateral and Depth Dimensions.

Figure 27 shows the effect of convolution between the generation volume region and the recombination luminescence. Without taking this into account, the diffusion length measured by the transport imaging will not be a correct interpretation of the actual minority charge carrier diffusion behavior.
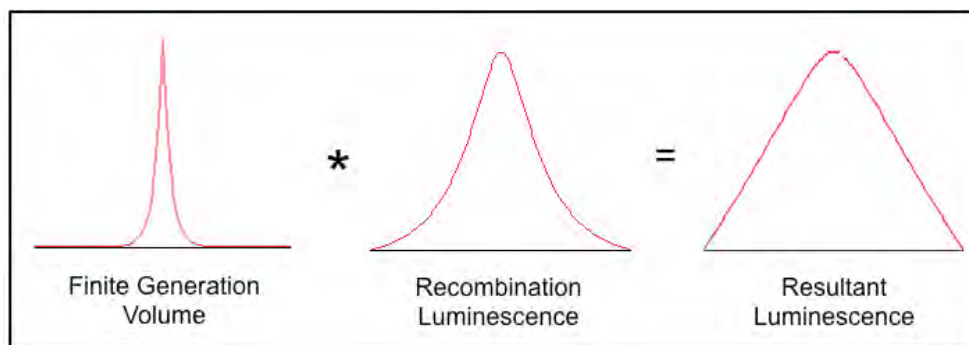
Figure 27. Convolution of the Generation Volume with the Recombination Luminescence

To overcome this limitation and obtain the true mobility values, there was a need to deconvolve the resultant luminescence back into its original components so that they could be evaluated independently.

B.   DECONVOLUTION MODEL

The ideal method was to perform a direct deconvolution process on the results to retrieve the actual recombination luminescence. To do this, there was a need to model the two components—both the generation volume and the diffusion behavior—in mathematical form.

In this first attempt, the finite charge carrier generation volume could be approximated as a region that followed a Lorentz distribution perpendicular to the line source and could be represented as:

$$L(x) = \frac{\gamma}{(x - x_0)^2 - \gamma^2}$$

Eq. (14)

where x is the horizontal position, x_0 is the center of the distribution, and γ is the Lorentz parameter characterizing the width of the generation region. Since the measurements were taken from the center, x_0 was set to 0 and Equation 14 reduced to:

$$L(x) = \frac{\gamma}{x^2 - \gamma^2}$$

Eq. (15)

From the information presented in Chapter III, the diffusion distribution from a point source could be described by:

$$I_N(x) = e^{\frac{-x}{L_{diff}}}$$

Eq. (16)

where x is the horizontal position and L_{diff} is the diffusion length.

The convolved result, R, of the carrier diffusion from the charge carrier generation volume region could now be represented as:

$$R(x) = \int_{-\infty}^{\infty} \frac{\gamma}{\xi^2 + \gamma^2} \bullet e^{-\frac{|x-\xi|}{L_{diff}}} \, d\xi$$

Eq. (17)

where ζ is the integration variable representing position in the diffusion axis.

It should be noted that while this would be the most direct method to independently determine L_{diff} and γ, it would require a two-parameter fit of the integrated term. Due to the difficulty of performing direct deconvolution, a proposed two-stage deconvolution process would be employed instead. This two-stage process involved the using of known data to first approximate the value of the γ parameter, and thereafter to calculate the diffusion lengths based on this approximated γ parameter. This process was proposed as a means of testing the viability of the deconvolution model while the actual multi-parameter fitting could be carried out in the future if the approach proved to be feasible.

C.   DECONVOLUTION PROCESS

1.   Stage I

The first stage sought to approximate an empirical description of the generation region due to the electron beam (i.e., the γ parameter of the Lorentz distribution), and then determine the diffusion length based on this starting point. To achieve this, the mobility value for one sample set had to be assumed in order to estimate the value of γ parameter. To reduce the uncertainty of the assumed mobility value, the sample with the supposed shortest diffusion length would be chosen. This would be the Set 04 samples.

In terms of minority charge carrier mobility values, Set 04 samples should theoretically be the lowest among all four sample sets. The first reason was that Set 04 samples were n-type materials, thus having holes as their minority charge carriers as opposed to electrons for the others. From Hall effect measurements [17], it has been shown that holes in InGaP have lower mobility than electrons, thus contributing to shorter diffusion lengths. The second reason was that it was also the sample set with the highest doping level. As discussed earlier in Chapter IV, a higher doping level generally reduces the diffusion length due to lower mobility and, in many cases, shorter lifetimes. Therefore, being an n-type material and being the heaviest doped sample set, Set 04 samples were expected to have the shortest minority carrier diffusion lengths.

Based on the Hall effect on the mobility of holes as majority charge carriers [18], the mobility value of holes as minority charge carrier was assumed to be 45 cm^{2}V^{-1}s^{-1}. With the measured lifetime data (τ = 2.28 ns), the diffusion length was calculated to be 0.52 µm.

Using the approximated diffusion length value for L_{diff} in Equation 17, different values of γ were substituted and the predicted intensity distributions of R were calculated (Figure 28). From the R distributions, linear regression was performed to obtain the gradient of the slope (Figure 29). The range of data used for the line-fitting was in the range of 0.4 to 0.8 for normalized intensity as this was the part where the curve stabilized and presented a relatively straight profile. The convolved diffusion lengths of these R results were then compared against the actual experimental result for Sample 4A to identify the case that gave the closest fit. The γ parameter value was then selected to be the γ value that gave this closest fitting result. After iterations of γ value substitution and comparison, the γ parameter value was determined to be 0.48 µm (Table 6).
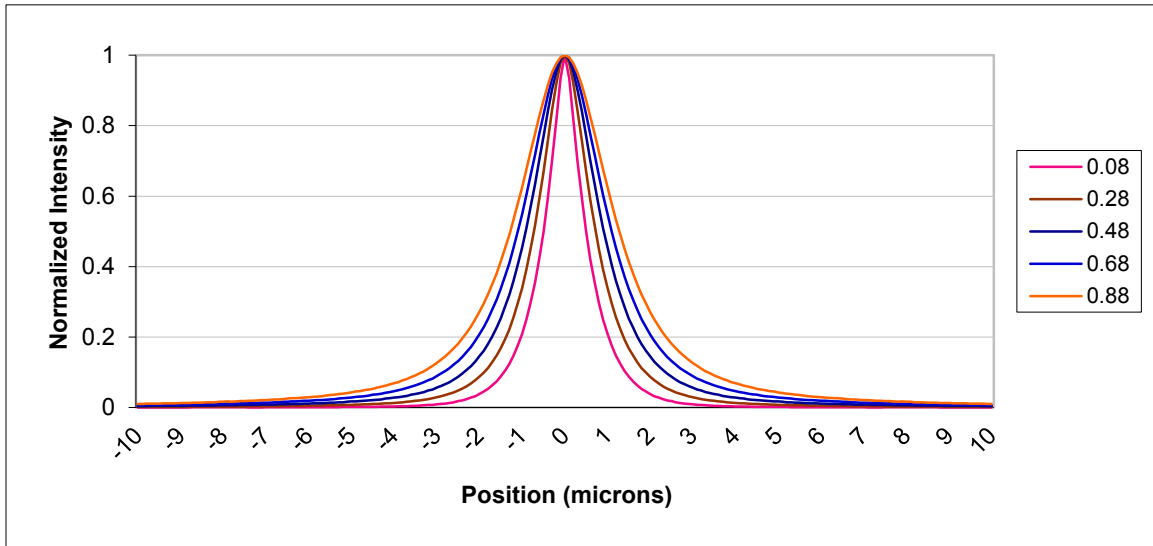
Figure 28.   Results for Different Values of the Lorentz Parameter
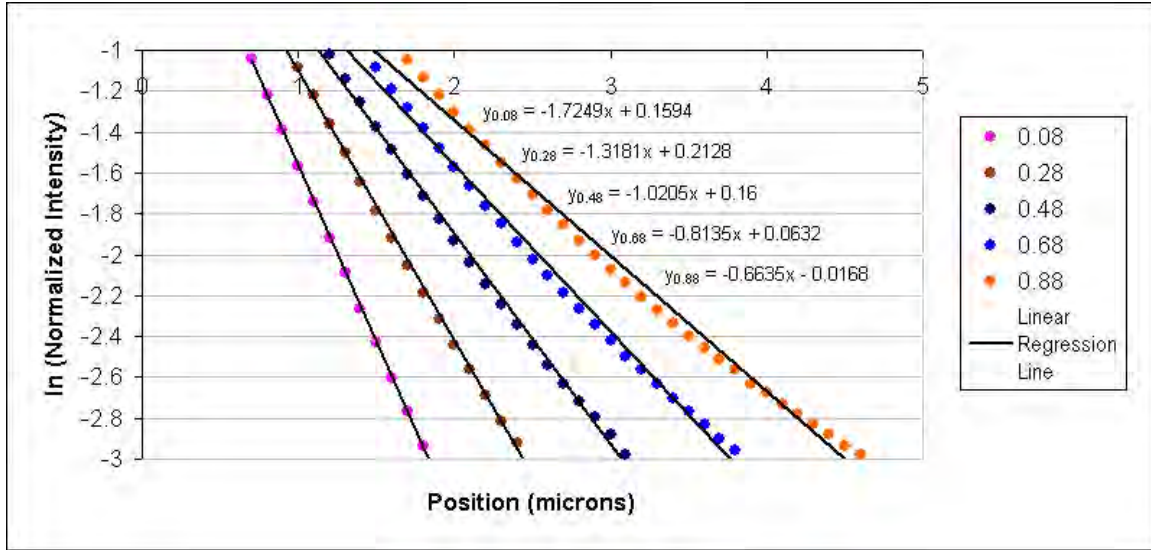
Figure 29.   Line-fitting for Extraction of Slope Gradient for Stage I

Lorentz Parameter (µm)		Slope Gradient (µm^{-1})	1/Slope Gradient (µm)		Experimental Diffusion Length (µm)
0.08		-1.725	0.58		
0.28		-1.318	0.76		
0.48		-1.021	0.98		0.98
0.68		-0.814	1.23		
0.88		-0.664	1.51		

Table 6.   1/Slope Gradient Results for Different Values of the Lorentz Parameter

2.   Stage II

Having determined the best estimated value of the γ parameter, the deconvolution model now became a one-parameter fit model—that of L_{diff}. Using the value of 0.48 µm for the γ parameter, the Lorentz distribution representing the generation volume was convolved with the exponential

distribution of the recombination luminescence with different values of L_{diff} for each sample. Similarly, the L_{diff} value for each sample was determined based on the value that gave the closest match with the actual experimental results. Figure 30 illustrates the different resulting distributions based on substituting different values of L_{diff} for Sample 3A and Figure 31 shows the line-fitting process for the extraction of the slope gradient of the distributions. The diffusion lengths of the resulting distributions for Sample 3A were then calculated and tabulated in Table 7. The case of L_{diff}, with a value of 1.22 μm, gave the closest match of the convolved diffusion length with that of experimental results. Therefore, the L_{diff} value for Sample 3A is determined to be 1.22 μm.
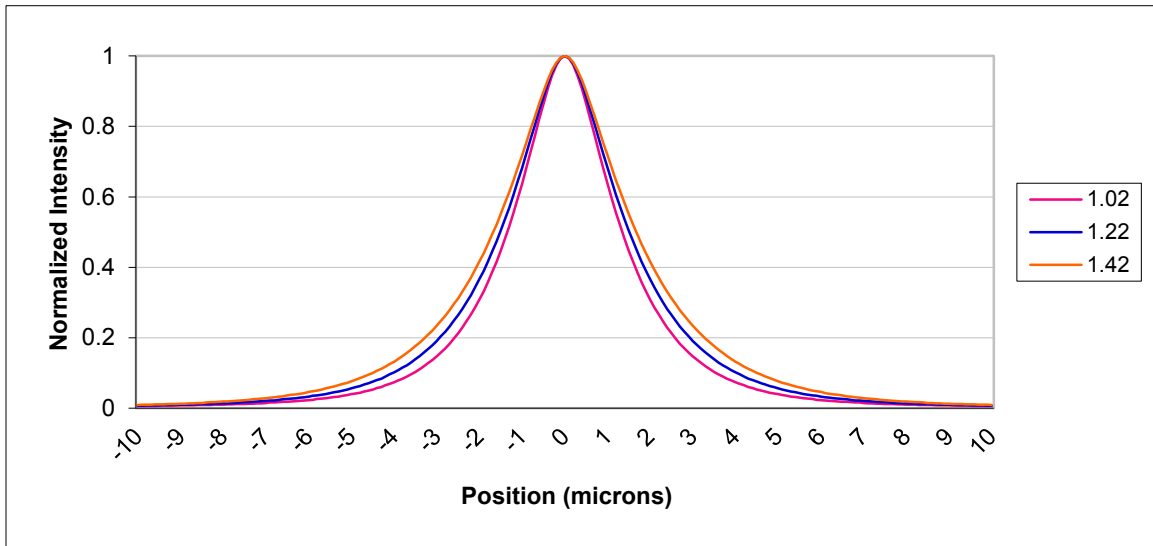
Figure 30. Results for Different Values of the Diffusion Length for Sample 3A
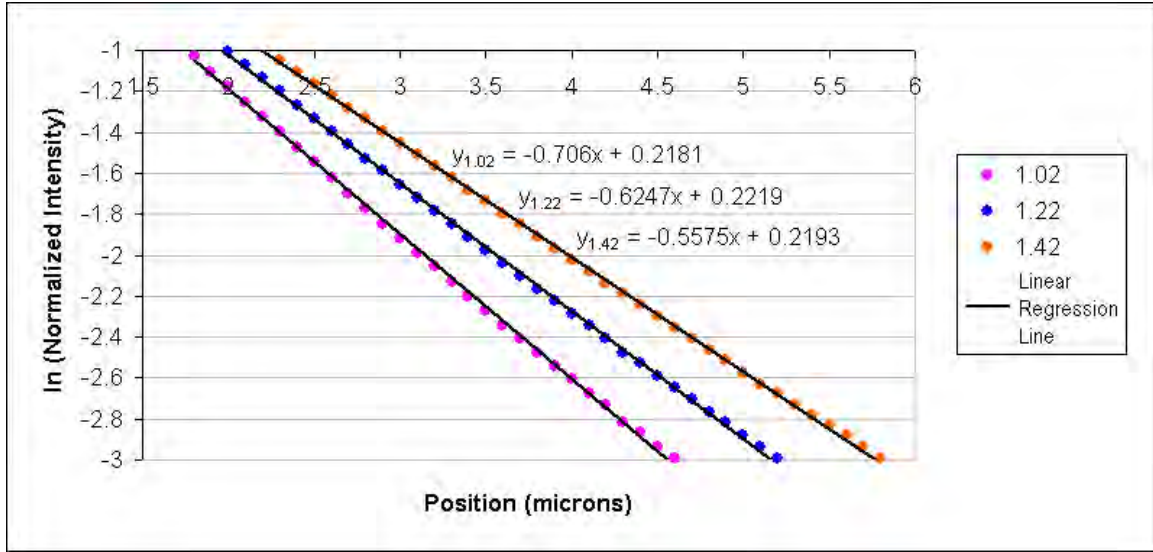
Figure 31.   Line-fitting for Extraction of Slope Gradient for Stage II

Actual Diffusion Length, (µm)		Slope Gradient (µm^{-1})	1/Slope Gradient (µm)		Experimental Diffusion Length (µm)
1.02		-0.706	1.42		
1.22		-0.625	1.60		1.60
1.44		-0.558	1.79		

Table 7.   1/Slope Gradient Results for Different Values of the Diffusion Length

D.   RESULTS AFTER DECONVOLUTION

The application of the deconvolution model was able to separate the effects of the finite charge carrier generation volume from that of the diffusion behavior, thereby obtaining more accurate diffusion lengths for each of the samples. The recalculated mobility of the minority charge carriers based on the deconvolved diffusion lengths were reduced in value and were now order-of-magnitude consistent with the limited expected values based on other techniques

54

in the literature. The deconvolved diffusion lengths and the recalculated minority charge carrier mobility values are summarized in Table 8.

Set #	Type	Thickness (µm)	Lifetime @ 300K (ns)	Uncorrected Diffusion Length @ 300K (µm)	Deconvolved Diffusion Length @ 300K (µm)	Uncorrected Mobility @ 300K (cm²V⁻¹s⁻¹)	Deconvolved Mobility @ 300K (cm²V⁻¹s⁻¹)
1	p-InGaP (higher doping – 1×10^{17} cm⁻³)	0.3	1.13	1.11	0.67	421	154
		0.5	1.03	1.00	0.56	375	118
		1.0	1.32	0.99	0.54	287	85
2	p-InGaP (lower doping- 5×10^{16} cm⁻³)	0.3	1.07	1.17	0.75	494	203
		0.5	0.83	1.12	0.68	584	215
		1.0	0.95	1.06	0.62	457	156
3	p-InGaP (lower doping – 5×10^{16} cm⁻³)	0.3	1.36	1.60	1.22	727	423
		0.5	1.37	1.30	0.90	477	228
		1.0	1.55	1.24	0.83	383	172

Table 8.   InGaP Minority Charge Carrier Mobility Results After Deconvolution

E.   SENSITIVITY TEST

A sensitivity analysis was also performed to determine the degree of variation in the results due to different assumptions for the starting value of the hole mobility for the deconvolution process. Earlier, the assumed value for the hole mobility was taken to be 45 cm2V-1s-1. For the sensitivity analysis, two new hole mobility values were used (one was double of the original value while the other was half the value) and the deconvolution process re-run to determine the new L_{diff} for the samples. The results based on the diffusion of Sample 3A are given in Table 9.

55

Assumed Hole Mobility @ 300K ($cm^2V^{-1}s^{-1}$)	Resultant Lorentz Parameter (μm^{-1})		Diffusion Length (μm)	Electron Mobility @ 300K ($cm^2V^{-1}s^{-1}$)
22.5	0.56		1.14	369
45.0	0.48		1.22	423
90.0	0.31		1.37	533

Table 9.   Sensitivity Testing of Sample 3A

From the sensitivity analysis results, it was observed that when the assumed hole mobility value was halved (i.e., 22.5 $cm^2V^{-1}s^{-1}$), the electron mobility value was decreased by 13%. Similarly, when the hole mobility was assumed to be double the base value (i.e., 90 $cm^2V^{-1}s^{-1}$), there was an increase of 26% to the mobility of the electrons. From a statistical point of view, the electron mobility could be considered rather sensitive to the starting value of the hole mobility used for the deconvolution process and could potentially vary by 13% to 26%. However, from an absolute value point of view, the results were deemed to be stable as the numerical change is small when compared to the mobility values of majority carriers, which are in the range of 1000 $cm^2V^{-1}s^{-1}$ or higher, and were order-of-magnitude consistent with the expected values from literature data.

F.   OBSERVATIONS

The range of the majority charge carrier mobility (for both electrons and holes) based on the Hall effect was also provided by the sample providers and is given in Table 10. A comparison between Table 8 and Table 10 showed that the mobility of the electrons as minority carriers was considerably lower than that of the electrons as majority carriers. This suggests that minority charge carrier mobility is lower than majority charge carrier mobility for a given carrier type in a

single material. The finding is consistent with theoretical work in GaAs, which predicts that minority carrier mobilities are lower by a factor of 0.6 and 0.9, depending on compensation [19].

Material	Majority Charge Carrier Type		Charge Carrier Concentration (cm^{-3})	Hall Mobility $(cm^2V^{-1}s^{-1})$
InGaP	Electron		1×10^{18}	800
			2×10^{18}	650
			5×10^{18}	500
			7×10^{18}	450
	Hole		2×10^{17}	45
			3×10^{17}	40
			8×10^{18}	27

Table 10.   InGaP Majority Charge Carrier Mobility Based on Hall Effect (From [18])

Based on the results of the sensitivity analysis, it was also shown that the deconvolution model was fairly successful in eliminating the effect of the generation volume from the recombination luminescence to allow the extraction of the actual diffusion length and, subsequently, the minority charge carrier mobility. Although the method presented in this thesis was a first attempt at the deconvolution process, it has demonstrated that the model is a feasible one and could prove more effective with further research.

THIS PAGE INTENTIONALLY LEFT BLANK

VI. TRANSPORT IMAGING OF CIGS

A. CIGS TECHNOLOGY

Copper Indium Gallium (di)Selenide, also known as CuInGaSe$_2$ or CIGS, represents an alternate semiconductor material choice that can be used for solar cell manufacturing. CIGS is a I-III-VI$_2$ semiconductor that is made of the elements copper, indium, gallium and selenium, as the name will have implied. The elements are tetrahedrally bonded in a chalcopyrite crystal structure to form the CIGS compound. It is a direct band-gap material with a band-gap range of 1.04 eV to 1.67 eV depending on the composition of indium and gallium mixture in the compound [20].

CIGS suffers from low energy-conversion efficiency when compared to other solar cell materials. Currently, the highest reported conversion efficiency stands at 20.3%, while the average efficiency attained for normal line production standard is at 10 to 12%. Alongside single-junction silicon-based solar cells with peak efficiency of 27.6% and an average of 16 to 17% efficiency, or more advanced multi-junction solar cells of 30 to 40% efficiency [21], CIGS pales in comparison.

CIGS does, however, have a few unique characteristics that are advantageous over other material types, and these are the reasons why solar cell producers are interested in research and commercial development of CIGS material.

One such advantage of CIGS over silicon-based or other material type semiconductors is that it has a very high absorption coefficient (10^5 cm^{-1} for 1.5 eV or higher energies) as compared to the rest [22]. Up to 99% of light incident of it is absorbed in the first 1 μm or so [23]. The implication is that only a thin film of CIGS is needed to absorb the same amount of sunlight compared to other semi-conductor materials with lower absorption coefficients.

Another advantage of CIGS is that it can be deposited on flexible substrates, such as polymide or metal foils [24]. Coupled with its high absorbing

characteristic, CIGS is an ideal choice for the manufacturing of thin-film flexible solar cells, which are relatively lightweight and can be easily portable. Unlike crystalline silicon, which produces rigid and delicate solar panels that require careful handling, these flexible and portable CIGS solar cells offer a myriad of product opportunities in both the commercial and military sectors. One possible application in the military domain is a CIGS solar cell mat that can be rolled up and carried by the average soldier during movement and can be easily set up to power devices, such as small-scale unmanned aerial vehicles (UAVs) or communication sets, during operations.

One deciding factor of choosing CIGS though, will be in terms of cost. CIGS is a relatively cheaper material to manufacture and install compared to mainstream solar cell materials, such as silicon or InGaP. This is due to its capacity of operating with polycrystalline, as opposed to higher-cost single-crystal materials, thus making it a lower-cost material. The CIGS technology of today is far from mature but with further research, the production cost of CIGS-based solar cells can be driven down even lower. Together with its other interesting characteristics of high absorbency and substrate flexibility, CIGS solar cells have the potential to grow and become a huge competitor in the solar cell industry.

B.   SAMPLES

Through collaboration with researchers in the solar cell field, three samples of CIGS solar cells were obtained for studying in this thesis work. These samples will be labeled as Sample C1, C2, and C3, respectively.

Transport imaging has been performed on these three samples with the objective of measuring their diffusion lengths and finding their minority charge carrier mobility value in order to understand their transport behavior better. As CIGS are p-type materials, the focus is the electron carrier mobility.

C.   SEM SETTINGS

For all the experiments on the CIGS samples, the SEM was set with the experimental configuration as given in Table 11:

SETTING	VALUE
Electron Beam Energy	20 keV
Probe Current	3×10^{-10} A
Magnification	x 1500

Table 11.   SEM Operating Parameters for CIGS Measurements

D.   INITIAL TRANSPORT IMAGING OF CIGS

The luminescence images of the CIGS samples using the transport imaging technique are given in Figure 32. In contrast to the luminescence seen in the earlier InGaP samples, the luminescence observed of the CIGS had less uniform distributions. The distorted luminescence pattern was either a reflection of material non-uniformity or a result of light-scattering caused by the rough and uneven surface of the material.
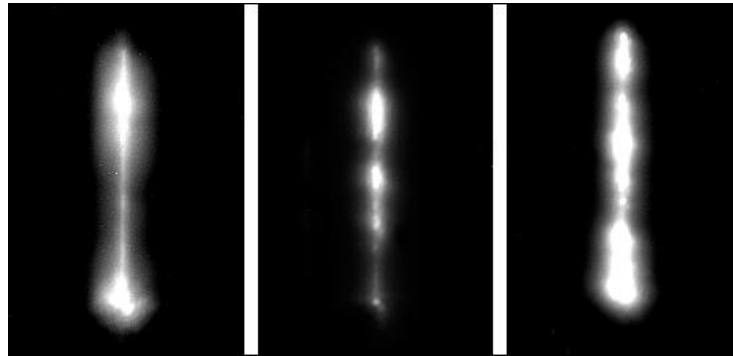
Figure 32.   Live-scan Luminescence Images of CIGS Samples [256 pixels (102 μm) x 172 pixels (68 μm) each]

In order to obtain a more accurate interpretation of the luminescence distribution, each of the luminescence images had to be separated into smaller parts (Figure 33). This allowed the luminescence to be localized to a region for study and the various regions could later be compared.
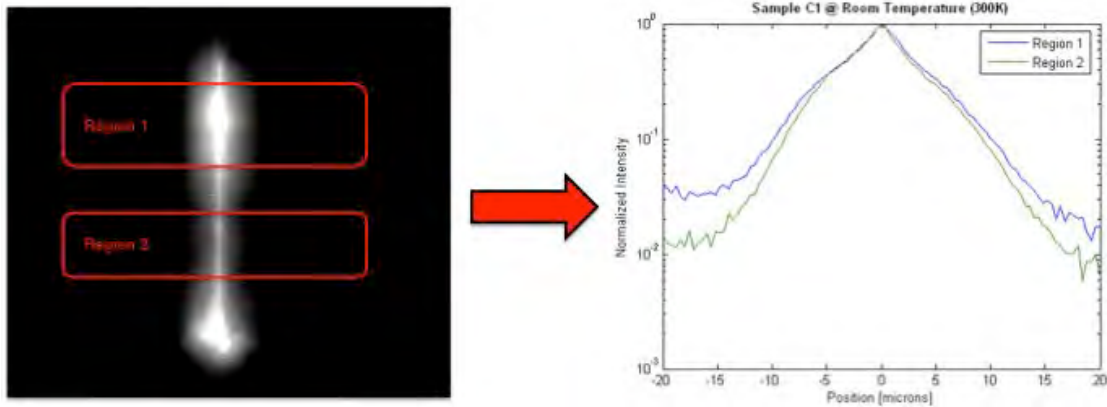
Figure 33. Localized Luminescence Distributions

Figure 34 shows a comparison of the obtained luminescence distributions of each of the samples. From the graph, it could be observed that Sample C1 had the widest distribution while Sample C2 had the narrowest.
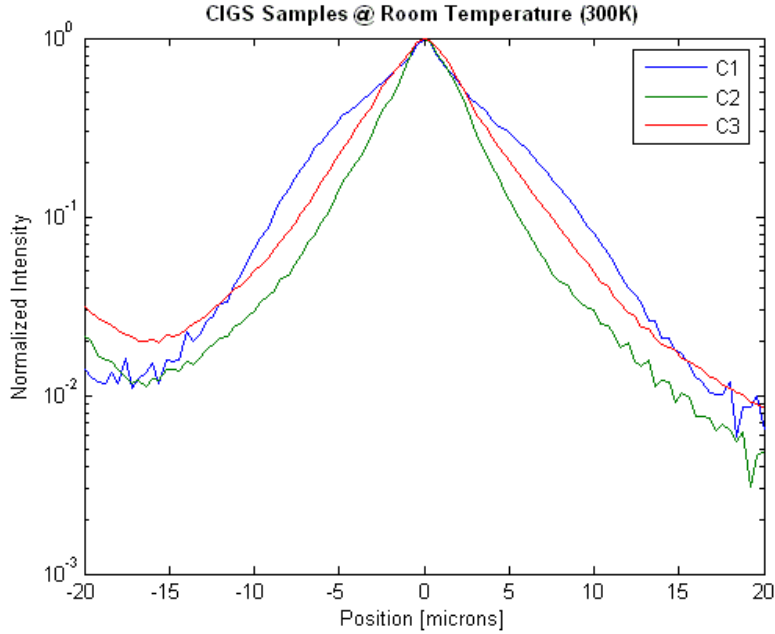
Figure 34.   Comparison of CIGS Luminescence Distributions

The line-fitting process is illustrated in Figure 35, where linear regression was performed in order to extract the gradient of the slopes.   For the CIGS material, a longer range of data could be used for the line-fitting due to its wider distributions as compared to those of the InGaP material.   In general, the position data (x-axis) used for the line-fitting was approximately in the range of 2 μm to 8 μm.   Using the gradient, the diffusion lengths of the samples were then calculated and tabulated in Table 12.
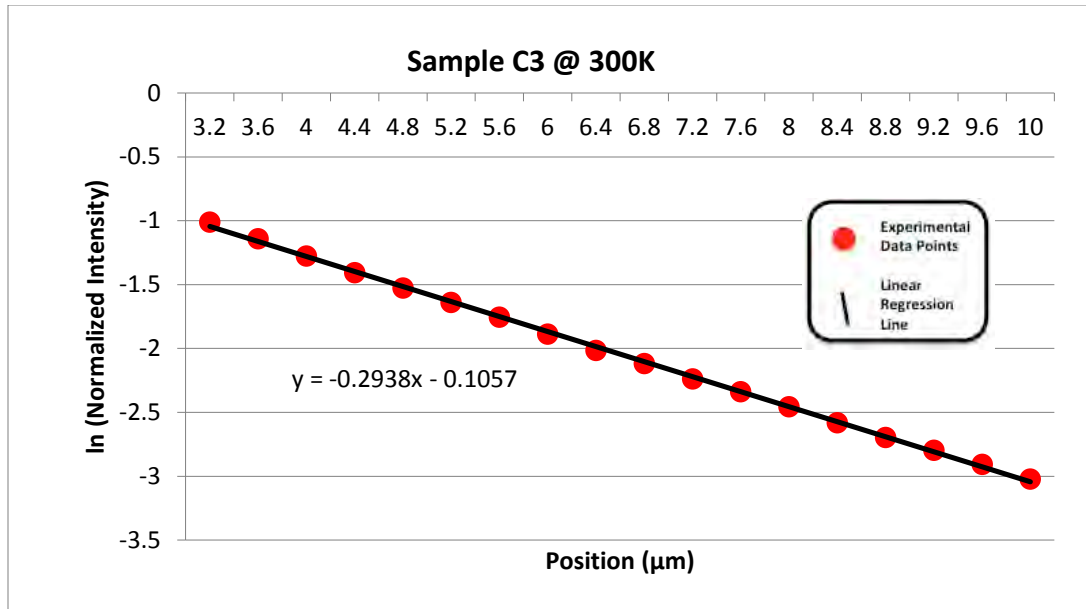
Figure 35. Plot of Ln (Normalized Intensity) as a Function of Position for Gradient Extraction for Sample C3

Samples		Shortest Diffusion Length (μm)	Longest Diffusion Length (μm)	Average Diffusion Length (μm)
C1		3.17	3.75	3.49
C2		2.29	2.76	2.46
C3		3.38	3.38	3.38

Table 12. CIGS Sample Diffusion Length Results

Independent TRPL lifetime data were also available from the sample providers, allowing the calculation of the minority charge carrier mobility, which is shown in Table 13. Unlike the InGaP samples, there was no need for deconvolution of the CIGS diffusion length. This was due to the fact that the diffusion lengths were longer for the CIGS (i.e., 2 μm and above), and thus were out of the affected region of the finite generation volume.

Samples		Average Diffusion Length (µm)	Lifetime (ns)	Mobility $(cm^2V^{-1}s^{-1})$
C1		3.49	4	1180
C2		2.46	6	390
C3		3.38	6	736

Table 13.   CIGS Minority Charge Carrier Mobility Results

E.   OBSERVATIONS

From this experiment, preliminary values for the minority charge carrier (electron) mobility of the CIGS material were established.   While the mobility values of samples C2 and C3 were within expectation; however, the mobility value of sample C1 seemed to be slighter higher than the norm.

From the collected luminescence images, it was clear that the surface roughness played a part in scattering the light source and distorted the eventual charge carrier generation process.   This resulted in the uneven recombination luminescence that was observed.   It was believed that in addition to the recombination luminescence, the CCD camera would have also received some of the back-scattered light.   These coupled signals would certainly affect the accuracy of the transport imaging technique and hence influence the subsequent determination of the diffusion length.   Therefore, these mobility values would just represent a first approximation of the CIGS transport behavior and should not be taken as absolute values.

THIS PAGE INTENTIONALLY LEFT BLANK

VII. CONCLUSION

A.   SUMMARY

Solar energy represents a unique solution to the world's increasing energy demands. To that end, higher-efficiency solar cells are required in order to be able to fully harness the energy from the sun. An understanding of the transport behavior of solar cell materials enables manufacturers to characterize the materials better and hence build more effective solar cell devices. The minority charge carrier diffusion length and mobility are two important transport parameters for such material characterization.

In this thesis, work was done to determine the minority charge carrier diffusion length of two materials, InGaP and CIGS, which represent two very different solar cell technologies in the market today. Transport imaging, a non-destructive and contact-free, optical imaging technique was applied to the two material samples in order to extract the diffusion lengths. Together with independent sets of TRPL lifetime data, the mobility of the minority charge carriers were subsequently determined.

For the InGaP sample set, the diffusion length was found to be in the range of 0.5 to 1.2 µm, while the mobility value of the minority charge carriers was found to be in the range of 80 to 400 $cm^2V^{-1}s^{-1}$. The mobility was lower in value as compared to that of the majority charge carriers which was obtained through the Hall effect. This result is consistent with the existing literature data of GaAs [19]. In addition, the experiments also showed how the diffusion length and mobility values were affected as a result of different material type, doping level, sample thickness, and the ambient temperature.

A limitation in the optical technique was encountered while experimenting on the InGaP samples. As the diffusion lengths of the InGaP samples were significantly short, the charge carrier recombination process was within the region of the finite generation volume. This caused the coupling of the two signals, which affected the initial measurements of the transport imaging. To

67

solve the problem, a deconvolution process, which modeled the convolution of the recombination luminescence with the generation volume, was proposed and presented. The process aimed to separate the two coupled components into their individual parts so that the recombination luminescence can be studied independently. Following the deconvolution process, both the diffusion lengths and minority carrier mobility values were lowered, allowing a more accurate measurement of the transport parameters.

For the CIGS samples, the diffusion length was found to be in the range of 2 to 4 μm, while the mobility value of the minority charge carriers was found to be in the range of 300 to 1400 $cm^2V^{-1}s^{-1}$. The challenge of applying transport imaging on the CIGS was that the rough surface of the samples tends to scatter the light source and distorts the final luminescence image collected by the CCD camera. As a result, the extracted diffusion lengths based on the distorted luminescence represented only an approximation rather than the actual value of the transport behavior in the material.

B   FUTURE RESEARCH

The deconvolution model presented in this thesis has the objective of separating two convolved signals into individual components so that the luminescence resulting from the material can be studied independently for a more accurate interpretation of the actual diffusion length. To do this, the beam source was modeled as a Lorentz function while the luminescence distribution was modeled as an exponential function. However, the model was a first-attempt effort, which used an approximation of the γ parameter for the Lorentz function representing the beam source. This approximation was based on the assumed value of 45 $cm^2V^{-1}s^{-1}$ for the hole carrier mobility. While the model worked and gave a better fit of the electron carrier mobility values, there is a certain degree of inaccuracy involved.

To address the problem, there is a need to determine the true value of the γ parameter, which characterized the beam source. One approach is to use

sample materials with known transport parameters (i.e., mobility and lifetime) for the testing of the model. The experimental diffusion length is a convolved product of the actual diffusion length and the Lorentz distribution. Since the actual diffusion length is known (as it can be calculated as a mobility-lifetime product), different values for the γ parameter can be fitted to see which gives the closest fit to the experimental result. Once the value of the γ parameter is determined, a direct deconvolution of the coupled signals can then be done instead of performing the two-stage process used in this work.

THIS PAGE INTENTIONALLY LEFT BLANK

LIST OF REFERENCES

[1]   J. Nelson, *The Physics of Solar Cells.* London, U. K.: Imperial College Press, 2007.

[2]   "Solar cell breaks efficiency record" [Online]. IEEE Spectrum, Available: http://spectrum.ieee.org/green-tech/solar/solar-cell-breaks-efficiency-record.Last modified August 11, 2011.

[3]   R. Mabus, "Environmental outlook: The military and alternative energy," National Public Radio transcript from July 5, 2011 [Online]. Available: http://www.navy.mil/navydata/people/secnav/Mabus/Interview/NPR%20Transcript%20-%20Operational%20Energy%20(5%20Jul%2011).pdf. Accessed November 11, 2011.

[4]   D. W. Snoke, "Excitonic circuits: New tools for manipulating photons," *Photonics Spectra,* January, 2006 [Online]. Available: http://www.photonics.com/Article.aspx?AID=23970. Accessed October 24, 2011.

[5]   Hyperphysics, "P- and n-type semiconductors" [Online]. Available: http://hyperphysics.phy-astr.gsu.edu/hbase/solids/dope.html. Accessed October 25, 2011.

[6]   J. W. Mayer and S. S. Lau, *Electronic Materials Science: For Integrated Circuits in Si and GaAs.* New York: Macmillon, 1990.

[7]   A. Sconza and G. Torzo, "A simple and instructive version of the haynes-shockley experiment," *European Journal of Physics,* vol. 8, no. 34, 1987. doi:10.1088/0143–0807/8/1/008.

[8]   W. K. Metzger *et al.*, "Time-resolved photoluminescence and photovoltaics," paper presented at the 2004 Department of Energy Solar Energy Technologies Program Review Meeting, Denver, Colorado, October 25–28, 2004.

[9]   S. O. Kasap, *Optoelectronics and Photonics, Principles and Practices.* New Jersey: Prentice Hall, 2001.

[10]   HowStuffWorks, "How solar cells work," [Online]. Available: http://science.howstuffworks.com/environmental/energy/solar-cell.htm. Accessed October 28, 2011.

[11]   R. R. King *et al.*, "New horizons in III-V multijunction terrestial concentrator cell research," presented at the 21st European Photovoltaic Solar Energy Conference and Exhibition, Dresden, Germany, September 4–8, 2006.

[12]   Renewable Energy UK. "Multi-junction solar cells" [Online]. Available: http://www.reuk.co.uk/Multi-Junction-Solar-Cells.htm. Accessed October 12, 2011.

[13]   T. Kato *et al.*, "Influence of lattice mismatch on photoluminescence from liquid phase epitaxial grown InGaP on GaAs substrates." *Journal of Crystal Growth,* vol. 71, iss. 3, 1985, pp. 728–734. doi:10.1016/0022–0248(85)90383–5.

[14]   N. M. Haegel *et al.*, "Direct transport imaging in planar structures," *Applied Physics Letters,* vol. 84, iss. 8, 2004. doi: 10.1063/1.1650544.

[15]   T. J. Mills, "Direct Imaging of Minority Charge Carrier Transport in Triple Junction Solar Cell Layers," M. S. thesis, Naval Postgraduate School, Monterey, California, 2006.

[16]   A. Chen *et al.*, "InAs/InGaP/GaAs heterojunction power schottky rectifiers," *Electronics Letters,* vol.. 42, iss. 7, 2006.

[17]   O. Madelung, *Semiconductors: Data Handbook* (3rd ed.). New York: Springer, 2003.

[18]   N. M. Haegel (private communication), 2011.

[19]   W. Walukiewicz *et al.*, "Minority-carrier mobility in p-type GaAs," *Journal of Applied Physics,* vol. 50, no. 7, 1979.

[20]   M. Gloeckler and J. R. Sites, "Band-gap grading in $Cu(In,Ga)Se_2$ solar cells." *Journal of Physics and Chemistry of Solids,* vol. 66, iss. 11, pp. 1891–1894, 2005.

[21]   Gigaom, "How CIGS solar can become mainstream" [Online]. Available: http://gigaom.com/cleantech/how-cigs-solar-thin-film-can-become-mainstream.Last modified March 4, 2011.

[22]   B. J. Stanbery, "Copper indium selenides and related materials for photovoltaic devices." *Critical Reviews in Solid State and Material Sciences,* vol. 27, iss. 2, pp. 73–117, 2002.

[23]   Solar Thin Films, "CIGS technology" [Online]. Available:
        http://www.solarthinfilms.com/active/en/home/photovoltaics/cigs_technolo
        gy.html. Accessed November 1, 2011.

[24]   N. G. Dhere, "Toward GW/year of CIGS production within the next
        decade." *Solar Energy Materials and Solar Cells,* vol. 91, iss. 15, 2007, p.
        1376. doi:10.1016/j.solmat.2007.04.003.

THIS PAGE INTENTIONALLY LEFT BLANK

INITIAL DISTRIBUTION LIST

1. Defense Technical Information Center
    Ft. Belvoir, Virginia

2. Dudley Knox Library
    Naval Postgraduate School
    Monterey, California

3. Professor Andres Larraza
    Chair, Department of Physics
    Naval Postgraduate School
    Monterey, California

4. Professor Nancy Haegel
    Naval Postgraduate School
    Monterey, California

5. Professor Sherif Michael
    Naval Postgraduate School
    Monterey, California

6. Ong Zi Xuan
    Republic of Singapore Armed Forces
    Republic of Singapore

7. Professor Yeo Tat Soon
    Director, Temasek Defence Systems Institute
    National University of Singapore
    Republic of Singapore

8. Tan Lai Poh
    Senior Manager, Temasek Defence Systems Institute
    National University of Singapore
    Republic of Singapore